UMHEP PUB - 401
NEVIS PUB - R#1497
FNAL PUB - 93/356

Pion-Pion Correlations at Low Relative Momentum Produced in p-p Collisions at 27.5 GeV/c.*

The BNL E766 Collaboration

Abstract

We have measured the momentum correlation of pion pairs produced in the collisions of 27.5 GeV/c protons in liquid hydrogen. By considering events for which all final state particles have been measured, we have succeeded in reducing backgrounds due to particle misidentification below 5% for π^+ and 1% for π^-. Our use of a precision magnetic spectrometer has provided an accurate determination of particle momenta and excellent acceptance for particle pairs with small relative momentum essential for correlations studies. A large data sample of fully reconstructed events (1 x 10^6) allows us to analyze the correlations for $\pi^+\pi^+$ and $\pi^-\pi^-$ pairs separately, and also as a function of the final state multiplicity. We find that the pion pair correlations scale 0.98 fermi, describes the data well. We do not find any indication of multiplicity dependence of the correlation scale for multiplicities from six to fourteen final state particles.

Submitted to Physical Review D, November 24, 1993

* Funded in part by the National Science Foundation under Grants PHY89-211320, PHY90-14879; the Department of Energy under Contracts No. DE-AC02-76CH03000, DE-AS05-87ER40356; and CONACyT de Mexico.

Pion-Pion Correlations at Low Relative Momentum Produced in p-p Collisions at 27.5 GeV/c.*

J. Uribe[(a)], E.P. Hartouni, D.A. Jensen[(b)], and M.N. Kreisler

Department of Physics and Astronomy, University of Massachusetts, Amherst, MA 01003

M.D. Church[(b)], E.E. Gottschalk[(c)], B.C. Knapp, W. Sippach, B.J. Stern[(d)], and L.R. Wiencke[(e)]

Columbia University, Nevis Laboratories, Irvington, NY 10533

D.C. Christian, G. Gutierrez, S.D. Holmes and A. Wehmann

Fermilab, Batavia, IL 60510

C. Avilez[(f)]

Instituto de Fisica, Universidad de Guanajuato, Leon, Gto., Mexico

M. Forbush[(g)], F.R. Huson, and J.T. White

Department of Physics, Texas A & M University, College Station, Texas 77843

[PACS:13.85.Hd,13.90.ti]

* Funded in part by the National Science Foundation under Grants PHY89-211320, PHY90-14879; the Department of Energy under Contracts No. DE-AC02-76CH03000, DE-AS05-87ER40356; and CONACyT de Mexico.

Abstract

We have measured the momentum correlation of pion pairs produced in the collisions of 27.5 GeV/c protons in liquid hydrogen. By considering events for which all final state particles have been measured, we have succeeded in reducing backgrounds due to particle misidentification below 5% for π^+ and 1% for π^-. Our use of a precision magnetic spectrometer has provided an accurate determination of particle momenta and excellent acceptance for particle pairs with small relative momentum essential for correlations studies. A large data sample of fully reconstructed events (1 x 10^6) allows us to analyze the correlations for $\pi^+\pi^+$ and $\pi^-\pi^-$ pairs separately, and also as a function of the final state multiplicity. We find that the pion pair correlations scale 0.98 fermi, describes the data well. We do not find any indication of multiplicity dependence of the correlation scale for multiplicities from six to fourteen final state particles.

I Introduction

The observation of relative momentum correlations between pairs of like sign pions in low energy proton - anti-proton reactions[1] was made in the late 1950's. A possible explanation of these correlations was proposed almost immediately in a paper by Goldhaber, Goldhaber, Lee and Pais[2] (referred to hereafter as GGLP). In that paper the agreement between the data and a properly symmetrized statistical model[3] calculation provided compelling evidence that the correlations were due to the bosonic nature of pions. GGLP showed that identical particles emitted by separated sources will have correlated momenta. The exact form of the two-particle relative momentum probability distribution depends on the detailed nature of the sources and their space-time configuration. GGLP assumed a simple Gaussian source distribution in the relative space-time position of the sources to ease calculational difficulties. This source distribution was then integrated over the "reaction volume" to provide a probability function which modified the pion kinematic variables. An assumption of the statistical model is that the square of the matrix element is independent of the kinematic variables of the initial state and final state particles. There is only one adjustable parameter in GGLP's analysis, the "radius" of the reaction volume.

Many other experiments observed pion correlations in low energy interactions during the 1960's[4]. The comparison of these experimental results with theory is less compelling than GGLP due to: the increasing complexity of the reactions, the existence of resonances, the existence of final state interactions, the increasing number of pions and the inability to calculate the correlations.

The possibility of using the pion correlations to measure the space-time development of the hadronic interaction was proposed by Kopylov and Podgoreski[5] (referred to hereafter as KP). This paper explored the effects of different source distributions on the correlations. More importantly, the idea of a "correlation function" containing information about the space time development of the source was introduced. It was conjectured that the correlation function could be extracted from the measurements by examining the ratio of the data plotted in the correlation variable (e.g. the relative momenta) to a distribution in the same variable of events produced identically to the data *except for the correlations*.

Experiments[6] since KP have attempted to build the non-correlated data sample either from the data (e.g. pairing pions from separate events, etc.) or from a Monte Carlo simulation of the data or from both. The ratio of correlated to uncorrelated distributions are then fit to a standard parameterization associated with the physical aspects of the pion sources. An enhanced probability of low relative-momenta pairs is usually interpreted as the observation of the effect. Experiments analyzed in this manner using a variety of beam and target hadrons agree on the typical scale of the reaction volume radius, 1 fermi.

Observing a change in the correlation may signal a change in the underlying dynamics of pion production. In particular, a change of state due to high energy density reactions of nuclei[7] might be observed as a change in the pion relative-momenta correlation scale. It is the dependence of the correlation scale on nuclear atomic number[8] which provides the best evidence that pion correlations are actually measuring the source size. Of course the behavior of the correlations depends on the details of the phase transitions. These details remain beyond the realm of our calculational ability.

There are several difficulties in observing correlations. The correlations in a sample can be "diluted" by the inclusion of misidentified particles. The existence of resonances which decay to pions can introduce kinematic correlations. Increasing the number of final state particles also increases the probability of final state interactions which will affect the correlation distributions. Finally, it is difficult to find uncorrelated samples with which to compare the correlated sample. This last difficulty affects the parameterization used to describe the correlation and its physical interpretation.

This study attempts to resolve many of those difficulties. We use a very large data set of approximately three hundred million events produced in proton-proton interactions. These data come from the BNL E766 experiment, which employed a multiparticle spectrometer capable of precise momentum measurements of high multiplicity (as many as 20 charged particles) reactions, and efficient charged particle identification, at high interaction rates (as high as 1 MHz).

The subset of data used in this study consists of events with two protons and charged pions for which all final state particles are measured. One million events satisfied these selection criteria. The size of this data sample allows us to separate the sample into final state multiplicities and pion pair charge. The ability to measure different final states within the same data sample reduces systematic uncertainties.

Doing the analysis as a function of pion pair charge provides a check on the effect of backgrounds due to particle misidentification. The characteristics of the charged pion sources should be independent of the pion charge, a consequence of the strong interaction charge invariance. Thus the distributions for positive charged pairs should be identical to those of negative charged pairs. In this experiment a major background to positively charged pions is misidentified protons. Particle identification is provided primarily by requiring the conservation of momentum and energy. Additional direct particle identification measurements reduce these backgrounds. Since negative pions cannot be mistaken for protons, the negative pion distributions provide checks on the positive pion distributions.

The pion pair correlations can be altered by the presence of resonances decaying to final states with charged pions. The measurement of all final state particles allows us to study the effects of resonance production on these correlations. Since all resonances produced in the interactions are observed (though not on an event-by-event basis) the effect of the resonance decay kinematics on the pion distributions can be studied from these data directly.

The effects of final state interactions on the correlations can be studied with the data. The precision of the momentum measurement allows for the observation of correlations between pions due to electromagnetic final state interactions[9]. The sensitivity of the apparatus to these small effects gives an indication of our sensitivity to final state interactions.

It is necessary to compare the correlation distributions to an uncorrelated sample. This study of data consisting of fully reconstructed events rules out a "traditional" procedure for constructing the uncorrelated data sample. Because energy-momentum conservation has been required for each event, replacing a pion in one event with a pion chosen randomly from another event would violate momentum-energy conservation for the event. We have chosen instead to compare the correlation distributions to "uncorrelated" distributions produced by Lorentz Invariant Phase Space (LIPS). This choice has two major advantages: 1) The procedure is simple to explain and interpret. And 2) the result is model independent. This second point is particularly compelling given the lack of either a calculable fundamental theory of interactions at these energies or of a believable empirical model. The statement of our results in terms of LIPS should allow a comparison with future calculations.

The use of fully reconstructed events presents some new complications in the analysis of pion correlations. However, using fully reconstructed events decreases particle identity backgrounds by *an order of magnitude* over studies using inclusive pion pairs. It is our opinion that this benefit outweighs the problems of a more complex analysis.

III The Apparatus

The BNL E766 apparatus was designed as a general purpose multiparticle spectrometer. The ability to reconstruct all of the charged particles from nucleon-proton interactions efficiently and precisely was a central design goal. To obtain large numbers of events to perform high sensitivity searches and precise, background free measurements required an apparatus capable of operating at high interaction rates for prolonged running periods.

The apparatus was located in the B-5 external beam line of the Brookhaven National Laboratory (BNL) Alternating Gradient Synchrotron (AGS). This beamline was configured to provide a high flux (10^{12}/sec) proton beam with a nominal momentum of 28 GeV/c. The beamline design minimized beam halo. The intensity of this beam was controlled by passing the beam through a wedge-shaped copper "degrader". The beam emerged from this "degrader" with a momentum of 27.5 GeV/c. The proton flux at the BNL E766 target was 10^7/sec. The beam had a 1-in. square profile at the target.

The momenta of the beam particles were determined by a set of four drift chambers and a string of dipole magnets. These were located between the "degrader" and the experiment's target. This beam spectrometer determined the incident beam proton's slope to $\pm10^{-4}$ radians horizontally and $\pm10^{-3}$ radians vertically. The momentum resolution of the beam spectrometer was ±300 MeV/c. The target region consisted of a "thin" (5% interaction length) liquid hydrogen target and a system of scintillation counters. These counters were used to detect the presence of a beam proton (and define the event's "initial" time) and to provide signals making it possible to veto on particles passing outside of the apparatus' geometric acceptance. Figure 1 depicts the target counter, target and veto box in relationship to the rest of the apparatus.

The multiparticle spectrometer consisted of five stations of drift chambers contained within the aperture of a large magnet (called the "Jolly Green Giant") and one drift chamber station located downstream of the magnet's aperture. Each drift chamber consisted of four planes oriented at ±7° and ±21° to the vertically oriented magnetic field. The drift chamber electrostatic structure was that of a PWC: alternating planes of cathodes and anodes. The anode-to-anode wire spacing varied from 2mm in the chamber closest to the target to 3.5mm in the furthest chamber. The 48 in. x 72 in. aperture of this last chamber subtended an angular acceptance of ±230 mrad. vertically and ±346 mrad. horizontally when measured from the center of the target 104 in. away. (The maximum possible acceptance is for a track passing through the 40 in. x 60 in. aperture of the third chamber located 36 in. away from the target: ± 507 mrad vertically and ± 695 mrad horizontally).

Details of the performance of the spectrometer are presented elsewhere.[10] We present here some important characteristics relevant to the correlation studies.[11] This spectrometer system achieved single plane efficiencies of greater than 99% allowing the efficient reconstruction of events with as many as 20 charged final state particles. The spatial resolution of each plane, when fully optimized, was in the range of 150-200 μm. Particles with momenta between 100 MeV/c and

28 GeV/c were measured with a $\Delta p/p = 0.0016p$ (GeV/c). The spectrometer was capable of distinguishing two track trajectories which shared common end points in the first and last chambers and were separated by as little as 4mm in the third and fourth chambers. The momentum resolution also provided a good measure of two particle relative momenta.

The particle momenta measurements are also used to establish that all final state particles are observed and to determine the identity of the final state particles. This is achieved through energy-momentum conservation relations described in detail below. Direct particle identification measurements provide a verification of the kinematically determined particle identities.

There are two detector systems in the apparatus which were used to make direct particle identification measurements: the time-of-flight (TOF) system and the Cherenkov system. The TOF system consisted of two counter hodoscopes: The Middle Hodoscope (MH) and the Rear Hodoscope (RH) (see Figure 1.). The Middle Hodoscope consisted of thirty plastic scintillator counters arranged in a picture frame around the "inner aperture" of the spectrometer. The Rear Hodoscope consisted of seventy-two counters covering the full downstream aperture of the magnet. Each counter was instrumented with a single photomultiplier tube. The scintillation light detected by each phototube was amplified. The pulse area and arrival time were measured by digitizing electronics[12]. This system achieved a 95% detection efficiency with a ±5pC measurement resolution of the time integrated signal current and a ±600ps (sigma) arrival time measurement. This provided a π-K separation to 1 GeV/c and a π-p separation to 1.6 GeV/c in the Rear Hodoscope and a π-p separation up to 0.75 GeV/c in the Middle Hodoscope.

The Cherenkov counter consisted of ninety-six cells, divided into sixty-four small "inner" cells and thirty-two large "outer" cells covering the downstream aperture of the magnet. This counter was filled with Freon 114 at atmospheric pressure. The Cherenkov radiation thresholds for π/K/p were 2.55/9.09/17.27 GeV/c. This detector provided high momentum particle identification. The high segmentation greatly reduced the confusion due to "crowded" particle clusters in high multiplicity events. The Cherenkov counter phototube pulses were measured with the electronics previously described. The pulse area was used to determine the number of photons emitted as Cherenkov radiation. The pulse arrival time information helped reduce the out-of-time backgrounds due to particle interactions in material surrounding the aperture of the apparatus.

The data acquisition system for this apparatus was designed to trigger and read out events at high rates. The general data driven architecture[13] allowed for a flexibly configurable trigger. The trigger and data acquisition system are shown in Figure 2.

The initial trigger indicated the presence of an event by scintillator coincidence. This trigger had a built-in deadtime of 30ns. A positive trigger from this coincidence initiated a more complex trigger decision, based on the sum of hodoscope counters with signal above threshold, special counters, or prescale count, i.e., event numbers. These conditions took no more than 60ns to calculate. A positive decision at this level initiated the digitization of the analog signal information, which had been "stored" by cable delay. The digitization and readout of zero-suppressed data then took an average of 1-2μs depending on event size. Once the data was read out, a third decision to keep the data was made using a Data Driven Processor[14] based on the number of clusters of hit wires in the drift chamber system -- a charged particle multiplicity trigger.

The surviving events were written into buffer memory and onto tape at roughly 3000 events per 1.5s spill. The average event size was 1 Kbyte. In a two week run, 3×10^8 events were written to 3000 nine-track 6250 bpi tapes.

IV Data Selection

The data sample used in the correlation study has the following characteristics: all final state particles are observed, all events are consistent with the hypothesis that all final state particles originate at a common vertex located within the liquid hydrogen target, and all final state particles are consistent with the hypothesis that only two are protons and the rest are either π^+ or π^-. The sample selected from the 3×10^8 event data set contains all the candidates for the reactions of the type:

$$
\begin{aligned}
p+p \to\ & p+p+2\pi^{+}+2\pi^{-} && (1a)\\
\to\ & p+p+3\pi^{+}+3\pi^{-} && (1b)\\
\to\ & p+p+4\pi^{+}+4\pi^{-} && (1c)\\
\to\ & p+p+5\pi^{+}+5\pi^{-} && (1d)\\
\to\ & p+p+6\pi^{+}+6\pi^{-} && (1e).
\end{aligned}
$$

Reactions with fewer than six charged particles were rejected by the multiplicity trigger. (Note that reactions with two and four particle final states cannot have two identical charged pions). Reactions with greater multiplicity than fourteen charged particles do not occur in the data with sufficient frequency to allow a statistically significant analysis to be performed. Table 1 summarizes the numbers of events in the samples for reactions (1a-e).

The data selection is performed in four analysis steps. At the first step the raw drift chamber data is used to reconstruct the trajectories of the charged particles through the magnetic field. This step is executed by a special purpose computer[14], the "hardware processor", with programmable selection criteria. The z-momenta of particles are summed for particles which have momentum less than 24 GeV/c. Events are then selected on the basis of the reconstructed track multiplicity (any event with more than eleven tracks is selected) and event summed z-momentum (any event for which the sum of the individual particle z-momenta sums to the initial beam z-momentum of 27.5 GeV/c within 5 GeV/c is selected). Roughly 50% of the sample survives these criteria.

The second reconstruction step finds any remaining trajectories and the vertices formed by the intersection of the tracks. This process begins by attempting to assign any unassigned wire "hits" to existing track trajectories. Those wire "hits" which remain unassigned are used to form additional candidate track trajectories. Once all trajectories are determined within the constraints of the pattern recognition algorithm, the intersections of these track trajectories are established. The determination of the primary vertex where the interaction occurred provides an additional space point which is used along with the drift chamber information to determine the track trajectories more precisely. Secondary vertices which occur downstream of the primary vertex are tested to determine if their identity is consistent with known, long lived particles (e.g. K_s^0 or Λ^0). For the purpose of the correlation study, only those events which are candidates for full event reconstruction are selected (the selection criteria are described below). The fraction of the data which survives reconstruction at this stage is 10% .

At the third step of the event reconstruction the incident beam particle trajectory and momenta are calculated. Kinematic constraints and conservation laws are imposed to obtain particle identification. The direct particle identification information is used to eliminate inconsistent assignments.

The fourth and final step of the analysis uses the events surviving the three reconstruction steps and various selection criteria. These criteria are used to isolate candidate events corresponding to reactions (1a-e).

It is important to demonstrate that the final data samples are free from background. We provide here more detail on the methods and effectiveness of the selection criteria. The kinematic constraints are applied in three cuts. The first cut requires that the square of the sum of final state particle momenta vectors perpendicular to the initial beam direction be consistent with the detector resolution. Figure 3 shows the distribution of the square of the sum of $\vec{p}_\perp$ for the events used in this study. Note the relatively flat distribution of events at large $\left(\sum \vec{p}_\perp\right)^2$. This is indicative of events with missing final state particles, with mismeasured beam momentum, or with mismeasured final state particles. The peak at small $\left(\sum \vec{p}_\perp\right)^2$ is due to events in which all final state particles have been measured. The width of this peak is ~(40 MeV/c)^2, consistent with Monte Carlo studies of the spectrometer's resolution. Events in this sample were required to have a $\left(\sum \vec{p}_\perp\right)^2$ less than or equal to 0.0016 (GeV/c)^2.

The conservation of longitudinal momentum (along the z-axis) forms the second cut. The difference of the beam momentum (measured by the beam spectrometer) and the sum of the momenta of the final state particles (measured by the spectrometer) is shown in Figure 4. The cut requires the momentum difference to be less than ±1 GeV/c. Since the standard deviation of the distribution in Fig. 4 is 300 MeV/c, it is a relatively loose cut.

In the third cut, the energy balance constraint is used to assign particle identities to the final state particles. Since low momentum tracks are measured more precisely than the high momentum tracks, energy conservation is not used directly. Instead, the sum of the energy minus the z-momentum is calculated for the initial and final states. We use the relationship:

$$E_i^2 = m_i^2 + p_{\perp i}^2 + p_{zi}^2,$$

where E_i, m_i, $p_{\perp i}$ and p_{zi} are the energy, mass, transverse momentum and z-component of the momentum for the i th particle.

This relationship can be rearranged as:

$$E_i - p_{zi} = \frac{m_i^2 + p_{\perp i}^2}{E_i + p_{zi}}. \quad (2)$$

Since the sum of E_i and p_{zi} are each individually conserved between the initial and final states, their difference is conserved. Using expression (2) eliminates the correlated error between E_i and p_{zi}. Figure 5 shows the distributions for the difference of the sums from initial to final state:

$$\Delta(E - p_z) \equiv \sum_{initial} \frac{m_i + p_{\perp i}^2}{E_i + p_{zi}} - \sum_{final} \frac{m_j^2 + p_{\perp j}^2}{E_j + p_{zj}}. \quad (3)$$

The fully reconstructed events have a $\Delta(E - p_z)$ distribution width of 4 MeV. The displacement of the distribution from zero probably results from small coordinate misalignments in the spectrometer. Note that expression (3) can be used to assign the final state particle identities by requiring that the masses m_j are selected to minimize $\Delta(E - p_z)$.

In addition to the kinematic constraints, only final states which satisfy the additive conservation laws (e.g. charge, strangeness, charm, baryon number, etc.) are considered. The effect of these cuts on the data sample are summarized in Table 1.

The level of backgrounds can be estimated for the isolated reactions (1a-e) and are shown in Table 2. The nature of backgrounds falls into three major categories: missing particles, incorrect identification of topology and incorrect assignment of particle identity within topology. The first category, missing particles, can occur when these particles have sufficiently low mass and momenta that they cannot be distinguished from momentum measurement variations due to the spectrometer resolution. In particular, π^0's dominate these backgrounds.

The second background category, incorrect identification of topology, is due to kinematic ambiguities unresolved by the direct particle identification measurements. For instance a $\pi^+\pi^-$ pair substituted for a K^+K^- pair may give a $\Delta(E - p_z)$ value within cut limits for *both* assumptions. If no additional information is available to determine the identity of these particles, the $\pi^+\pi^-$ solution is assumed to be correct.

The third category, incorrect assignment of particle identity within topology, occurs when the assignment of particle identity is ambiguous. For example, if the z-momentum for the two tracks is large, then the $\Delta(E - p_z)$ will remain the same (within resolution) independent of the assignment of masses to these tracks. The possible identity of these tracks is ambiguous and two solutions exist for the event. If no direct particle identification measurements are available to resolve the ambiguity, either assignment is possible. Figure 6 shows the momentum distribution for particles whose identity is ambiguous between π^+ or p. The effect of the TOF system direct identification measurement can be seen as a slight decrease of the distribution below 1 GeV/c. The Cherenkov measurement resolves the ambiguity for particle momenta above 2.5 GeV/c. The events used in the pion correlation studies contain equal numbers of π^+ and π^-. The π^- cannot be confused with any other particle in the event. All negative particles are pions. This fact allows us to determine the effect of ambiguous p-π^+ identity by comparing the π^- distributions to the π^+ distributions.

The background estimates presented in Table 2 are calculated by accounting for all of the fully reconstructed events. This is done for each topology separately. The total number of fully reconstructed events, N_{fm}, is determined by a fit to the $\left(\sum \vec{p}_\perp\right)^2$ distribution, (Fig. 3). (The fit function, determined empirically, is the sum of two exponential distributions and a linear polynomial, describing the signal and background, respectively.) This fit also provides the number of events with missing particles or mismeasured particles, N_{mm}. The sum of these two numbers equals the number of events in the topology:

$$N = N_{fm} + N_{mm}.$$

The total number of fully reconstructed events can be calculated by summing the number of events for each fully reconstructed topology. This number is determined by fitting the $\Delta(E\text{-}P_z)$ distribution for each topology, (Fig. 5):

$$N_{fm} = M_a + M_b + M_c + \ldots,$$

where M_a is the number of fully reconstructed events for topology a, M_b for b, etc. (The fit function used here is the sum of two Gaussian distributions and a quadratic polynomial, describing the signal and background, respectively.) For the topologies corresponding to reactions (1a-e) the dominant fully reconstructed backgrounds are those for which a $\pi^+\pi^-$ pair is replaced by a K^+K^- or $p\bar{p}$ pair. The fits to the topologies which include K^+K^- and $p\bar{p}$ pairs provide the number of these events which are backgrounds to the associated $\pi^+\pi^-$ topologies. For the topologies corresponding to reactions (1a-e) we would write:

$$B = M_{KK} + M_{p\bar{p}} + N_{mm} + A_{\pi p},$$

where B is the background, M_{KK}, $M_{p\bar{p}}$ are the number of fully reconstructed events with K^+K^- and $p\bar{p}$ pairs replacing $\pi^+\pi^-$ pairs, and $A_{\pi p}$ is the number of events with π^+-p ambiguities for the topology. For a given topology we also have the relation:

$$N = M_a + B_a,$$

where B_a is also determined in the $\Delta(E\text{-}p_z)$ fit which determines M_a.

Table 2 lists these quantities obtained by fits for the five topologies studied. In all cases the sum of individual background "components" exceeds the background determined by the fits of $\Delta(E\text{-}p_z)$. This is because the background categories are not exclusive. Note that for all topologies except the six-track topology, the dominant background contribution is from π^+-p ambiguities.

The worst topology, sixteen-track, has a 17% background for π^+. All topologies have less than 5% backgrounds for π^-. Note also that the number of fully reconstructed events, determined by a direct fit of $\left(\sum \vec{p}_\perp\right)^2$, agree well with the sum of fully reconstructed events found for each topology as determined by fits to $\Delta(E\text{-}p_z)$.

V. Data Analysis

a. Production Characteristics

Reactions (1a-e) have production characteristics which vary with multiplicity as a result of both kinematic and dynamic effects. Knowledge of these production characteristics is essential because they determine the particle momenta distributions. The correlations caused by kinematic limits as revealed in the particle momentum distributions must be distinguished from correlations caused by dynamical and statistical sources.

Our description of the production characteristics is based on the single particle momentum distributions for each reaction (1a-e). Figure 7 shows the laboratory momentum distributions for protons in these reactions. The selection criteria at the first reconstruction stage reduces the acceptance for high momentum protons. The low momentum cutoff is due to the finite backward (in the center-of-mass frame) acceptance of the spectrometer and the requirement that the entire event be observed. The proton momentum distributions in the interaction's center-of-mass frame are shown in Figure 8. It is readily apparent that for the low multiplicity reactions, the protons are isolated from each other. We interpret this as evidence for diffractive behavior. As the multiplicity increases, the proton momentum distributions change to resemble the "phase space" distributions. This appears to be a dynamical effect rather than a kinematic one. This behavior is also seen in other final states produced at these energies[10]. The proton rapidity distributions are shown in Figure 9 and the $p_\perp^2$ distribution in Figure 10. The $p_\perp^2$ distributions suggest that the low multiplicity events are diffractive (narrowly peaked in $p_\perp^2$) and the high multiplicity events are centrally produced. The Peyrou plots of Figure 11 also show this striking separation of protons for the low multiplicity events.

The π^+ and π^- laboratory momentum distributions are shown in Figure 12. The differences between the π^+ and π^- distributions are pronounced at low lab momentum. At low momentum, there is a high probability of confusing the p and π^+ and there is a large Δ^{++} production cross section for these reactions. The $\Delta^{++} \rightarrow p\pi^+$ decay tends to be a source of soft pions since the Δ^{++} decay kinematics require that the proton receive much of the Δ^{++} momentum.

The interaction center-of-mass frame momentum distributions (Figure 13) for the π^+ and π^- indicate that the pions are produced with small momenta in the center-of-mass. The distributions have asymmetric tails because of the finite backwards acceptance of the spectrometer.

Both the center-of-mass momentum distributions and the rapidity distribution (Figure 14) narrow as the multiplicity of the reaction increases. This effect is due to kinematics: less energy is available to individual pions as the number of pions increases. The kinematic limits are also seen in the $p_\perp^2$ distributions for the pions (Figure 15) which become narrow as the multiplicity increases.

The Peyrou plots (Figures 16 and 17) show the effect of the geometric acceptance on backwards pions, as well as the decreasing kinematic range, as the multiplicities increase.

Monte Carlo studies indicate that many of these observations can be explained by the mixing of two simple models (diffractive production and longitudinal phase space). The relative importance of each of these models depends on the final state multiplicity.

b. Correlations

The experimental signature of pion correlations due to Bose-Einstein statistics (referred to as Bose-Einstein correlations) is an increased probability of finding two identical particles with the same momenta. The range of relative momenta for which the probability is enhanced is related to the space-time separation of the particle sources. However, the actual distribution of two identical particles' relative momenta can be determined by both kinematic and dynamic phenomena. Both strong and electromagnetic final state interactions can play significant roles. In most cases direct calculations of the distribution shapes are not possible.

Correlation analyses[6] usually assume that independent sources of equal strength are described by a Gaussian distribution in space *and* time. This model of two particle production harks back to the original GGLP model, however inappropriate the original statistical model has become for describing particle production. Until better theoretical guidance is forthcoming, these parameterizations provide a way of organizing the existing data.

We define the relative four-momentum squared of two pions:

$$\begin{aligned} Q^2 &= -(P_1 - P_2)^2 \\ &= M_{12}^2 - 4m_\pi^2 \\ &= -\left(2m_\pi^2 - 2E_1E_2 + 2p_1p_2\cos\vartheta_{12}\right), \end{aligned}$$

where P_1 and P_2 are the four-momenta of pions *1* and 2, M_{12} is the invariant mass of particles *1* and *2*, m_π is the pion mass, E_1, E_2 and p_1, p_2 are the energy and momentum of pions *1* and *2* , respectively.

The two like signed pion Q^2-distributions for the reactions (1a-e) of this data sample are shown in Figures 18 and 19. The narrowing distribution width with increasing multiplicity is primarily a kinematic effect, as observed previously in the single particle longitudinal momentum distributions.

The data distribution is then compared to a distribution lacking the correlation. Ideally, the comparison distribution should contain *all other physics*. The ratio of the data distribution to the ideal comparison distribution results in the "correlation function", which is the Fourier-transformed source distribution. The validity of this procedure and the physical interpretation of the resulting parameterizations will be taken up in another paper[15]. The distribution ratios can be parameterized in the form:

$$R\left(Q^2\right) = 1 + \alpha\, e^{\beta Q^2},$$

where the ratio is unity at large Q^2, and $1+\alpha$ at small Q^2. In the original GGLP paper α was unity and β was related to the inverse square of the reaction volume radius.

The creation of the comparison distribution is a central problem for all analyses of Bose-Einstein correlations. In this study, the use of fully reconstructed events pose additional constraints. These constraints originate from the need to calculate the effects of geometric acceptance and reconstruction efficiencies on the comparison samples. Thus, the comparison sample should be generated with the correct dynamics, with the proper kinematic effects, but lacking the pion correlations. This daunting task is not currently achievable from fundamental principles nor from empirical models of particle reactions at these energies. Instead of developing an empirical model whose applicability might be limited and whose validity might be difficult to affirm, we propose an *Ansatz* to the standard parameterization. We use as a comparison distribution Lorentz Invariant Phase Space (LIPS). We further assume that the standard correlation function is modulated by a "source function":

$$R\left(Q^2\right) = \left(1 + \alpha\, e^{\beta Q^2}\right) S\left(Q^2\right),$$

where $S(Q^2)$ contains the large Q^2 behavior of the distributions, presumably due to the dynamics of pion production.

There is no theoretical argument to presume the separability of the correlation and source functions or the form of the source functions. However, other experiments[16] have required more complex parameterizations of the correlation function. Those parameterizations resemble our *Ansatz*.

c. Comparisons to LIPS

Our comparison sample is generated using Lorentz Invariant Phase Space. Events for each of the reactions (1a-e) are produced with a uniform density in their respective phase space volumes. The events are unconstrained in angular momentum. The generator model assumes a point-like interaction of spinless particles which produces point-like, spinless particles. We assume that the effects of spin and angular momentum in reactions (1a-e) average to the spinless case. These events are passed through a detector simulation program which produces "raw" data in the format of a "real" event. The analysis of these simulated events then follows the procedures used to analyze the real events.

The resulting π^+ and π^- single particle longitudinal momentum distributions are shown for each reaction (1a-e) in Figure 20. The multiplicity dependence of these distributions is similar to that seen in the data distributions (Figure 12). The major difference between the LIPS and real pion momentum distributions is due to the difference in the transverse momentum distribution. The dominant dynamical effect of pion production at these energies is the limiting of transverse momentum scale of the produced particles. Of course LIPS has no such limitation. This will cause the LIPS generated events to have a narrower distribution of longitudinal momentum than the data. The LIPS generated data show the same increase in the number of π^+ to π^- as was observed in the actual data. This increase is due to the π^+-proton identification ambiguities and Δ^{++} production.

Figures 21 and 22 show the two pion Q^2-distributions for the LIPS generated data. Once again, the kinematic narrowing with increasing multiplicity can be seen. Both these distributions and the data distributions (Fig. 18) are the result of an identical analysis procedure. Neither distribution has been "corrected". The bin-by-bin ratio of these distributions is shown in Figure 23, where "like sign" pair distribution ratios can be compared with the "unlike sign" pair ratio. The distribution ratios for each topology are normalized so that the ratios can be compared directly. The detector Q^2 resolution estimated from the Monte Carlo is not worse than $\Delta Q^2/Q^2 \leq 7\%$ for the smallest Q^2 bin.

In Figure 23 the $\pi^+\pi^+$ and $\pi^-\pi^-$ distributions seem to be the same throughout the Q^2 range. We conclude from this that $p-\pi^+$ ambiguities do not play an important role in the shape of these distributions. There are overall normalization differences which we will discuss later in this paper. The $\pi^+\pi^+$, $\pi^-\pi^-$ and $\pi^+\pi^-$ distributions are similar at large Q^2. This observation indicates that the "source dynamics" seem to be independent of the sign of the pions, as is expected based on charge independence of the strong interaction.

At low Q^2 there are large differences between "like" and "unlike" sign ratios. The unlike sign distributions display resonance structure at the invariant masses of the ρ (770) and f_2 (1270). There are no $|Q|=2$ meson resonances. Thus no resonance structure (due to two pion resonances) is seen in the like sign ratios. However, the like sign ratios show a significant increase compared to the unlike sign ratios as Q^2 goes to zero. This can be taken as a clear indication of a low Q^2 probability enhancement for identical particles, as expected from Bose-Einstein correlations. The increase in the smallest Q^2-bin for the unlike sign ratio is significant but is due to electromagnetic final state interactions. This will be discussed in the next section.

We also note that the like sign ratio low Q^2 enhancement does not vary dramatically with reaction. The high Q^2 behavior does vary both because of the change in the kinematic limits as a function of multiplicity and because of dynamics. This latter conclusion is due to the decrease with increasing multiplicity of the prominence of resonances produced per interaction in the unlike sign distributions. The phase-space for resonance-production is not markedly different (for these resonances) for the reactions (1a-e).

d. Other Final State Interactions

The correlations due to Bose-Einstein statistics for pions has the same effect as an attractive final state interaction. But pions will have other interactions with each other and with other particles in the final state due to both strong and electromagnetic forces. There is an attractive I=2 interaction between two like sign pions which is expected to be weak[17]. The observed enhancements seen in Figure 23 are larger than could be explained by this interaction. The electromagnetic final state interaction, also known as the "Gamow effect"[18] is repulsive for the like sign case and attractive for the unlike sign case. The increase of the lowest Q^2 bin in the unlike sign ratio is due to this attractive final state interaction[9]. The scale of these interactions is much smaller than the other Q^2 structures. Such an effect cannot be seen in the like sign case (where a "dip" would be expected). The effect for the repulsive case does not have a large integrated value for this Q^2 region. In the attractive case the effect diverges. Since the scale and magnitude of the electromagnetic interaction are very small for these data, we have not corrected the data for the effect.

In conclusion, the known two-body final state interactions do not provide a convincing explanation for the behavior of the Q^2 distribution ratios observed in Figure 23.

e. Resonances

Resonances are ubiquitous in these data. Aside from the prominent $\rho(770)$ and f_2 (1270) seen in Figure 23, there are pi-nucleon resonances Δ^{++}, N*(1512), N*(1675), etc. Pions which are decay children of these resonances could affect the scale of the Bose-Einstein enhancement, since their source, the strong resonance, has a typical decay proper length of 1 fermi. It is conceivable that the source distributions for pion decay children would be different than for "directly produced" pions. Certainly any explanation of pion source distributions would have to incorporate the effects of resonance production on the source distributions.

A more interesting idea is the possibility that the low Q^2-correlations observed in Figure 23 are *entirely* due to the presence of resonances. There are no data for which all of the final state pions are "outside" of resonances. Taking all two-particle invariant mass combinations, and excluding events with combinations within a resonance region (mostly ρ and Δ^{++}), yielded 151 events out of 139265 for reactions of the type (1a). The existence of resonances could cause a momentum correlation between like sign pions. Consider the Dalitz-plot of two-pion mass distributions for reaction (1a). If we index the pion combinations $\pi_1^+\pi_2^-$ and $\pi_3^+\pi_2^-$ then we know the amplitudes must be symmetric under the exchange of indices *1* and *3*. The observed invariant mass distribution should show the $\rho(770)$ (for example) for both combinations. Displayed in this Dalitz-plot, the ρ will appear as two bands, on a two dimension plot of m_{12}^2 vs. m_{23}^2. The "overlap region", the point where both π_1^+ and π_3^+ form a ρ with π_2^-, will be four times more populated than the "bands" outside of this region. This effectively correlates the momenta of π_1^+ and π_3^+, since the intensity for combining to a ρ is larger than what would be expected by random combinations. This symmetrization of resonance amplitudes will occur for all possible resonances.

The scale of the correlations would be on the order of the decay proper-length of these resonances. Although the initial study of the correlations, GGLP, did not observe an effect due to resonances (their center-of-mass energy was too low to produce significant numbers of resonances), it is possible that the higher energy, higher multiplicity experiments could be sensitive to the effects of resonance production[19].

The difficulties in understanding resonance effects stem primarily from a lack of a good formalism with which to calculate the pion momentum distributions from a large number of wide resonances. We are continuing to study these effects, which will be the subject of a future paper.

VI. Correlation Parameterization

a. Functional Forms.

We have used two functions to fit the ratio distributions of Fig. 18 for the like sign pions. These two differ only in the "correlation function". The same source parameterization is used. These functions are the "Gaussian correlation":

$$R\left(Q^2\right)=\left(1+\alpha\, e^{\beta Q^2}\right)\left(\lambda\left(1+\frac{\gamma}{\left(1+Q^2/\delta\right)^2}\right)\right), \qquad (4)$$

and the "Bowler correlation":

$$R_B=\left(1+\frac{\alpha}{\left(1+Q^2/\beta\right)^2}\right)\left(\lambda\left(1+\frac{\gamma}{\left(1+Q^2/\delta\right)^2}\right)\right). \qquad (5)$$

The "Bowler correlation" was motivated by considerations found in Ref. 20. The "source function" is the Fourier transform of an exponentially decreasing radial distribution of pion pairs. For both of these functions λ is the high Q^2 value of ratio being fit. Both functions have five parameters. The parameters are determined by a χ^2 minimizing fit for the ratio histograms shown in Figure 23. The central bin value is used as the Q^2 for the fit. The large statistics of this sample allow us to assume that the errors are calculated from the square root of the bin values in the numerator and denominator distributions and their ratio fractional error is the square root of the sum of the square of the individual fractional errors. The correlation among the parameters of these functions for the fits was found to be insignificant, but the errors quoted for the fit values include such correlations.

b. Results for Different Multiplicities.

The results for the fits are shown in Tables 3-6 and plotted in Figures 24 and 25. The data are "crosses" with the horizontal bar indicating the bin width and the vertical bar the error. The χ^2 per degree-of-freedom for these fits is typically 1, indicating that the functions (4) and (5) are consistent descriptions of the ratios. Note that these fits are over the full Q^2 range of Figure 23.

As a general observation, the "source function" parameters are in agreement between the two sets of parameterizations. This supports the assumption that the "source" and "correlation" functions can be factored. The different correlation function Q^2-dependencies indicate that there is little correlation between the parameters of the "source" and "correlation" functions in the fitting procedures.

The parameters for the Bowler and Gaussian correlation functions have quite similar behaviors. The term multiplying the Q^2 dependent part of the correlations, sometimes referred to as the "strength" term, is larger for $\pi^-\pi^-$ than for $\pi^+\pi^+$ ratios. This could be due to the "dilution" of the π^+ data by ambiguous protons and resonance production.

The parameters α and β from the fits are plotted in Figures 26 and 27. The scale parameter β can be interpreted as source separation length scales for each parameterization. Thus, for the Gaussian correlation function :

$$rms\ radius = \hbar c\sqrt{3\beta}$$

and for the Bowler correlation function :

$$rms\ radius = \hbar c\sqrt{6/\beta}\,.$$

These are shown in Figures 28 and 29. The $\pi^+\pi^+$ and $\pi^-\pi^-$ distributions are in excellent agreement with each other. No multiplicity dependence is required to explain the data.

VII Comparisons With Other Data

Table 7 lists the results of this experiment together with those of other experiments. In all cases the errors quoted are statistical. Cases for which the initial particles are both protons seems to cluster around a radius of 1 fermi. However the errors, if taken as an actual indication of an experiment's ability to measure the radius parameters, would indicate that these results are not consistent with each other. Differences could be due to a dependence of the radius with center-of-mass energy. Aside from the highest energy point, the radius seems to be increasing with energy.

The differences might also be attributed to the production mechanism. Such a dependence is supported by the fact that changing the species of the initial particles affects the measured radius.

Multiplicity dependence is studied in other experiments also. High energy pp and $p\bar{p}$ interactions and nuclei-nuclei collisions observe multiplicity dependencies. This multiplicity dependence was parameterized in the variable $\Delta n / \Delta\eta$, (charged multiplicity observed in the pseudo-rapidity region) in Reference 21 at $\sqrt{s} = 630$ GeV as:

$$R_G = 1.03 + 0.089\frac{\Delta n}{\Delta\eta}\ fermi.$$

This dependence agrees qualitatively with other high energy experiments[22] and with the results of nuclei-nuclei collisions[10]. The data from this study are presented in Table 8 for each charge species and reaction type. Also tabulated are the pion multiplicity for the reaction and the full width half maximum (FWHM) of the pion rapidity distributions in that reaction. The ratio of pion multiplicity to rapidity distribution FWHM is given as $\Delta n/\Delta\eta$. These radii data are then fit using three hypotheses: 1) the data are constant in multiplicity, 2) the data depend linearly on n, the pion multiplicity, and 3) the data depend linearly on $\Delta n/\Delta\eta$. The first hypothesis results in radii:

$$R_G(++) = 0.982 \pm 0019 \quad fermi \quad \chi^2/dof = 3.7/4$$
$$R_G(--) = 0.987 \pm 0.024 \quad fermi \quad \chi^2/dof = 2.7/3,$$

which agree with each other and have good fits. The second hypothesis results in the fits:

$$R_G(++) = (0.773 \pm 0.019) + (0.020 \pm 0.012) \times n$$

$$\chi^2/dof = 0.998/3$$

$$R_G(--) = (0.899 \pm 0.112) + (0.008 \pm 0.014) \times n$$

$$\chi^2/dof = 2.2/2,$$

which also give good fits. The slope parameters for both fits are not inconsistent with zero slope. The third hypothesis resulted in:

$$R_G(++) = (0.882 \pm 0.065) + (0.024 \pm 0.015) \times \frac{dn}{d\eta},$$

$$\chi^2/dof = 1.2/3;$$

$$R_G(--) = (0.935 \pm 0.071) + (0.012 \pm 0.015) \times \frac{dn}{d\eta},$$

$$\chi^2/dof = 2.1/2.$$

Once again, the fits seem to be good and the slope terms consistent with zero slope. We conclude that these data do not require a multiplicity dependence to be explained. The absence of a multiplicity dependence of the radius at low center-of-mass energy agrees with the observation of Reference 23. Figure 30 shows these data in comparison with other experiments as a function of the multiplicity dependence $\Delta n/\Delta\eta$, assuming that rapidity and pseudorapidity are equivalent.

VIII Conclusions

This study of two pion correlations isolated a large number of totally reconstructed events identified as reactions

$$\begin{aligned} p+p &\rightarrow p+p+2\pi^+ +2\pi^- && (1a)\\ &\rightarrow p+p+3\pi^+ +3\pi^- && (1b)\\ &\rightarrow p+p+4\pi^+ +4\pi^- && (1c)\\ &\rightarrow p+p+5\pi^+ +5\pi^- && (1d)\\ &\rightarrow p+p+6\pi^+ +6\pi^- && (1e). \end{aligned}$$

Two distinguishing characteristics of these data are the high momentum resolution achieved by the spectrometer and the small backgrounds due to missing particles and particle misidentification.

Using this well defined sample of reactions and comparing the two pion relative four-momentum (Q^2) distribution, we observed low Q^2 -enhancements for both $\pi^+\pi^+$ and $\pi^-\pi^-$ consistent with each other and not inconsistent with measurements made by other experiments. Taking the hypothesis that these enhancements are the consequence of Bose-Einstein symmetry for the pions, the scale of the enhancement can be interpreted as the interaction volume radius, measured to be 0.98 fermis both from $\pi^+\pi^+$ and $\pi^-\pi^-$ correlations. The interaction volume radius also appears to be independent of multiplicity for these data.

These results are consistent with previous observations, though the technique and data sample used by this study differ greatly from those used in other analyses of pion correlations.

Acknowledgments

We express our gratitude to A. Pendzick and his AGS crew for their support throughout our run at BNL. We are thankful for the patience and care provided by D. Quilty, who assembled this manuscript, and to the editorial skills of A. Therrien. We would also like to acknowledge seminal discussions with B. Klima, and the helpful discussions with M.S.Z. Rabin during the course of the analysis. We have all been enriched by our association with Clicerio Avilez and are saddened by his untimely death. We hope that the analysis of the experiments to which he dedicated his untiring efforts will provide an equally rich legacy.

FOOTNOTES:

(a) Present Address: University of Texas, M.D. Anderson Cancer Center, Houston, Texas 77030

(b) Present Address: Fermilab, Batavia, Illinois 60510

(c) Present Address: Carnegie-Mellon University, Pittsburgh, Pennsylvania 15213

(d) Present Address: AT&T Research Laboratories, Murray Hill, New Jersey 07974

(e) Present Address: University of Utah, Salt Lake City, Utah 84112

(f) Deceased

(g) Present Address: University of California, Davis, California 95616

1 G. Goldhaber, *et al.* Phys. Rev. Lett. **3**, 181 (1959)

2 G. Goldhaber, *et al*, Phys. Rev. **120,** 300 (1960)

3 E. Fermi, Prog. Theorl Phys. **5**, 570 (1950)

4 N. Xuong and G.R. Lynch, Phys. Rev. **128**, 1849 (1962)
T. Ferbel, *et al*, Phys. Rev. **143**, 1096 (1966)
V. Alles-Borelli, *et al* Nuovo Cimento **50A**, 776 (1967)
R.A. Donald, *et al*, Nucl Phys **B6**, 174 (1968)
R.A. Donald, *et al*, Nucl Phys **B11**, 551 (1969)

5 G.E. Kopylov and M.K. Podgoretskiy, Sov. J. Nucl. Phys **15,** 219 (1972)

6 for a comprehensive review of the experimental situation see D.H. Boal, C-K Gelbke, and B.K. Jennings Rev. Mod. Phys. **62**, 553 (1990)

7 S. Pratt Phys. Rev. **D33**, 1314 (1986)
G.F. Bertsch Nucl. Phys. **A498**, 173c (1989)

(continued next page)

FOOTNOTES (continued)

8 see for instance W.A. Zajc, Nucl. Phys. **A525**, 315c (1991)

9 L.R. Wiencke, *et al*, Phys. Rev. **D46**, 3708 (1992)

10 Spectrometer performance article in preparation. Details can be found in the Theses:

Michael Church, "Ξ^- Production in 15-28 GeV Neutron-Proton Interactions", Nevis-260. Columbia University, Nevis Laboratories (1986).

Benjamin Stern, "A Search for Charmed Particles in 15-28 GeV Neutron-Proton Interactions". Columbia University, Nevis Laboratories (1988), Nevis-266.

Michael J. Forbush, "High Mass Diffractive Dissociation at 27.5 GeV Proton-Proton Interactions in Exclusive Final States", Texas A&M University (1990).

Erick E. Gottschalk, "Strange Baryon Production in 27.5 GeV/c Proton-Proton Interactions". Columbia University, Nevis Laboratories (1992), Nevis-278.

Lawrence R. Wiencke, "Observation of Final State Coulomb Interactions in Proton-Proton Collisions at 27.5 GeV/c", Columbia University, Nevis Laboratories (1993), Nevis-280.

Jorge Uribe Duque, "Pion Pion Correlations at Low Relative Momentum Produced in the Reactions $pp \to pp(\pi^+\pi^-)^n$ with n = 2, 3, 4, 5, 6", University of Massachusetts, Amherst (1993), UMAHEP-385.

11 The z-axis of the coordinate system is defined as the nominal beam direction. The y-axis is the vertical, "up" being the direction of increasing y. The beam right direction defined x-axis, explicitly this is $\hat{z} \times \hat{y}$. The coordinate system origin is set at the center of the magnetic field of the analyzing magnet.

12 E.P. Hartouni, *et al* Nucl. Instr. Meth. A **317**, 161 (1992)

Time-of-flight system performance paper in preparation

(continued next page)

FOOTNOTES (continued)

13 J.A. Crittenden, *et al*, IEEE Trans. on Nucl. Sci. **NS-31,** 1028 (1984)

E.P. Hartouni in "Workshop on High Sensitivity Beauty Physics at Fermilab" Nov. 11-14, 1987, Fermilab p415. (UMAHEP-291)

14 B.C. Knapp and W. Sippach, IEEE Trans. on Nucl. Sci. **NS27,** 578 (1980)

E.P. Hartouni, *et al*, IEEE Trans. on Nucl. Sci. **36**, 1480 (1989)

B.C. Knapp Nucl. Instr. Meth. **A289,** 561 (1990)

15 E.P. Hartouni and J. Uribe, "Interpreting Experimental Parameterizations of Bose-Einstein Correlations" in preparation

16 see for instance T. Åkesson, *et al*, Phys. Lett. **B155**, 128 (1985)

17 M.G. Bowler, Z. Phys. **C39**, 81 (1988)

18 B. Gamow, Z. Phys. **51,** 204 (1928)

19 H.Q. Song, *et al* Z. Phys. **A342**, 439 (1992)

20 M. Adamus, *et al* Z. Phys. **C37,** 347 (1988)

21 C. Albajar *et al*, Phys. Lett. **226**, 410 (1989)

22 See for example T. Alexopoulos, *et al*, "A Study of Source Size in $p\bar{p}$ Collisions at $\sqrt{s} = 1.8\,TeV$ Using Pion Interterometry" Fermilab E735 Preprint

23 A. Breakstone, *et al*, Z. Phys. **C33**, 333 (1987)

24 J.L. Bailly *et al*, Z. Phys. **C43**, 341 (1989)

25 M. Aguilar-Benitez, *et al*, Z. Phys. **C54**, 21 (1992)

26 H. Aihara, *et al*, Phys. Rev. **D31**, 996 (1985)

TABLES

1. Total numbers of events of the reaction types (1a-e) as a function of the final selection criteria.
2. Estimates of backgrounds for reactions (1a-e) designated by multiplicity.
3. Parameter values for function (4), "Gaussian correlation", fit to $\pi^+\pi^+$ Q^2-ratios for reactions (1a-e).
4. Parameter values for function (5), "Bowler correlation", fit to $\pi^+\pi^+$ Q^2-ratios for reactions (1a-e).
5. Parameter values for function (4), "Gaussian correlation", fit to $\pi^-\pi^-$ Q^2-ratios for reactions (1a-e).
6. Parameter values for function (5), "Bowler correlation", fit to $\pi^-\pi^-$ Q^2-ratios for reactions (1a-e).
7. Comparison of reaction volume radius with other experiments.
8. Multiplicity dependence of interaction radius as a function of the number of pions (n_π) and number of pions per unit rapidity ($dn/d\eta$).

Figures

1. A perspective view of the BNL E766 spectrometer. The drift chamber stations are labeled A - F.
2. Block diagram of BNL E766 data acquisition system.
3. $(\Sigma \vec{p}_{\perp i})^2$ distribution of six-track single vertex events which are candidates for the topology of reaction (1a).
4. Distribution of the difference between the beam momentum and the sum of the final state longitudinal momentum. Fully reconstructed events are defined to lie between the cuts indicated by arrows.
5. The $\Delta(E - p_z)$ distributions for events which are candidates for reaction (1a). The effect of cuts imposing transverse momentum conservation and agreement with direct particle identification are indicated. Arrows indicate final sample cuts.
6. The p_z -distribution of positive charged particles whose identity could be either proton or π^+ for reaction (1b).
7. Proton laboratory p_z momentum distributions for reactions (1a-e).
8. Proton center-of-mass p_z momentum distributions for reaction (1a-e).
9. Proton rapidity distributions for reactions (1a-e).
10. Proton transverse momentum squared distributions for reactions (1a-e).
11. Proton Peyrou plots for reactions (1a-e).
12. π^+ (solid line) and π^- (shaded line) lab frame longitudinal momentum distributions for reactions (1a-e).
13. π^+ (solid line) and π^- (shaded line) center-of-mass longitudinal momentum distributions for reactions (1a-e).
14. π^+ (solid line) and π^- (shaded line) rapidity distributions for reactions (1a-e).

15. π^+ (solid line) and π^- (shaded line) transverse momentum distributions for reactions (1a-e).

16. π^+ Peyrou plots for reactions (1a-e).

17. π^- Peyrou plots for reactions (1a-e).

18. $\pi^+\pi^+$ and $\pi^-\pi^-$ Q^2-distributions for reactions (1a-e).

19. $\pi^+\pi^+$ and $\pi^-\pi^-$ Q^2-distributions in the low Q^2 region for reactions (1a-e).

20. π^+ (solid line) and π^- (shaded line) lab frame longitudinal momentum distributions for reactions (1a-e) generated by LIPS Monte Carlo.

21. $\pi^+\pi^+$ (solid line) and $\pi^-\pi^-$ (shaded line) Q^2-distributions for reactions (1a-e) generated by LIPS Monte Carlo.

22. $\pi^+\pi^+$ (solid line) and $\pi^-\pi^-$ (shaded line) Q^2-distributions in the low Q^2 region for reactions (1a-e) generated by LIPS Monte Carlo.

23. Ratio of $\pi^+\pi^+$(shaded line), $\pi^-\pi^-$(shaded line), and $\pi^+\pi^-$ (solid line), Q^2-distributions data-to-LIPS Monte Carlo for reactions (1a-e).

24. $\pi^+\pi^+$ Q^2-ratios with fit of function (4), "Gaussian Correlation", superimposed for reactions (1a-e). Plots on right show low Q^2-region expanded, the lower fit curve is the "source function".

25. $\pi^-\pi^-$ Q^2-ratio with fit of function (4), "Gaussian correlation", superimposed for reactions (1a-e). Plots on right show low Q^2-region expanded, the lower fit curve is the "source function".

26. α and β parameter ("strength" and "radius") values from fits of function (4), "Gaussian correlation", to $\pi^+\pi^+$ (box) and $\pi^-\pi^-$ (cross) Q^2-ratios for reactions (1a-e). The $\pi^+\pi^+$, $\pi^-\pi^-$ combined are indicated by the circle.

27. α and β parameter ("strength" and "radius") values from fits of function (5), "Bowler correlation", to $\pi^+\pi^+$ and $\pi^-\pi^-$ Q^2-ratios vs. final state multiplicity. The $\pi^+\pi^+$, $\pi^-\pi^-$ combined are indicated by the circle.

28. Interaction volume radius from fits of function (4), "Gaussian correlation", plotted vs. final state multiplicity. The $\pi^+\pi^+$ data are indicated by the box, $\pi^-\pi^-$ by the cross and $\pi^+\pi^+$, $\pi^-\pi^-$ combined by the circle.

29. Interaction volume radius from fits of function (5), "Bowler correlation", plotted vs. final state multiplicity. The $\pi^+\pi^+$ data are indicated by the box, $\pi^-\pi^-$ by the cross and $\pi^+\pi^+$, $\pi^-\pi^-$ combined by the circle.

30. Dependence of interaction radius on $\frac{dn}{d\eta}$ for wide variety of beam and target particles and center-of-mass energies. The open symbols are data from this study.

	multiplicity (2+2m)					total
	6	8	10	12	14	
one vertex events	209512	1051449	581092	129761	16680	1988494
events after cut of $(\Sigma\vec{p}_\perp)^2$ $\leq 0.0016\ (\mathrm{GeV/c})^2$	129615	717663	394255	87277	10264	1339074
events with at least one pp $m\pi^+ m\pi^-$ solution and $-8 \leq \Delta(E-P_z) \leq +13$MeV	81549	542263	319818	74171	8973	1026774
events after direct particle identification	73770	469363	267307	61608	7689	879737
number of pp $m\pi^+ m\pi^-$ solutions/event	1.07	1.19	1.24	1.29	1.36	

			multiplicity (2+2m)				
			6	**8**	**10**	**12**	**14**
selected events			73710	469363	267307	61608	7689
Number of pp $m\pi^+m\pi^-$ solutions			75789	495097	291520	69398	8810
$\Delta(E\text{-}P_Z)$ signal, M_a			71445	452547	255417	58683	7273
$\Delta(E\text{-}P_Z)$ background, B_a			4236	41868	35711	10614	1515
background sources	kinematic ambiguities $A_{\pi p}$		2019 (2.6%)	25734 (5.2%)	24213 (8.3%)	7790 (11.2%)	1121 (12.7%)
	other exclusives	$p\bar{p}$, M_b	47 (.06%)	292 (.06%)	73 (.02%)	<88 (<.1%)	<9 (<.1%)
		K^+K^- M_c	473 (.6%)	3318 (.6%)	2410 (.8%)	<1719 (<2.5%)	<515 (<6.8%)
	mismeasurements $(\Sigma\bar{p}_\perp)^2$ background, N_{mm}		2637 (3.4%)	18171 (3.6%)	12202 (4.2%)	2914 (4.2%)	411 (4.6%)
$(\Sigma\bar{p}_\perp)^2$ signal, N_{fm}			73766	482344	282558	67317	8516
Signal balance			0.3%	0.1%	0.1%	1.2%	1.4%
Background balance			18%	11%	8%	0.8%	1%

Gaussian Parameter	pp $2\pi^+2\pi^-$	pp $3\pi^+3\pi^-$	pp $4\pi^+4\pi^-$	pp $5\pi^+5\pi^-$	pp $6\pi^+6\pi^-$
α	0.152 ±0.113	0.333 ±0.021	0.453 ±0.015	0.451 ±0.021	0.189 ±0.053
β	-34.590 ±37.760	-22.550 ±2.119	-24.580 ±1.321	-26.160 ±1.811	-51.570 ±29.770
γ	22.600 ±10.230	10.180 ±0.521	3.125 ±0.045	1.521 ±0.026	1.414 ±0.109
δ	1.893 ±0.123	1.360 ±0.032	0.978 ±0.024	0.583 ±0.030	0.198 ±0.024
λ	0.109 ±0.049	0.176 ±0.009	0.382 ±0.006	0.559 ±0.007	0.684 ±0.009
χ^2/DOF	111.9/95	128.4/95	99.2/95	106.1/95	125.6/95

Bowler	Final State				
Parameter	pp $2\pi^+2\pi^-$	pp $3\pi^+3\pi^-$	pp $4\pi^+4\pi^-$	pp $5\pi^+5\pi^-$	pp $6\pi^+6\pi^-$
α	1.669 ±20.790	0.431 ±0.029	0.601 ±0.020	0.645 ±0.036	0.257 ±0.205
β	0.004 ±0.028	0.061 ±0.009	0.061 ±0.005	0.066 ±0.007	0.035 ±0.045
γ	22.480 ±10.450	10.860 ±0.692	3.064 ±0.052	1.329 ±0.044	1.308 ±0.382
δ	1.884 ±0.128	1.443 ±0.043	1.098 ±0.038	0.709 ±0.056	0.209 ±0.071
λ	0.110 ±0.050	0.161 ±0.011	0.367 ±0.007	0.549 ±0.008	0.683 ±0.012
χ^2/DOF	113.3/95	120.7/95	87.8/95	105.2/95	126.5/95

Gaussian Parameter	pp $2\pi^+2\pi^-$	pp $3\pi^+3\pi^-$	pp $4\pi^+4\pi^-$	pp $5\pi^+5\pi^-$	pp $6\pi^+6\pi^-$
α	0.343 $\pm$0.077	0.439 $\pm$0.023	0.533 $\pm$0.015	0.553 $\pm$0.022	0.321 $\pm$0.057
β	-24.030 $\pm$7.564	-24.190 $\pm$1.837	-19.910 $\pm$0.905	-25.140 $\pm$1.445	-42.970 $\pm$12.930
γ	25.160 $\pm$27.580	9.062 $\pm$0.673	2.983 $\pm$0.078	1.472 $\pm$0.026	1.294 $\pm$0.091
δ	2.731 $\pm$0.312	1.724 $\pm$0.049	1.332 $\pm$0.045	0.714 $\pm$0.040	0.266 $\pm$0.036
λ	0.083 $\pm$0.093	0.179 $\pm$0.013	0.363 $\pm$0.009	0.548 $\pm$0.008	0.664 $\pm$0.012
χ^2/DOF	104.6/95	113.5/95	123.2/95	88.1/95	76.6/95

Bowler	Final State				
Parameter	**pp $2\pi^+2\pi^-$**	**pp $3\pi^+3\pi^-$**	**pp $4\pi^+4\pi^-$**	**pp $5\pi^+5\pi^-$**	**pp $6\pi^+6\pi^-$**
α	0.473 $\pm$0.186	0.577 $\pm$0.037	0.715 $\pm$0.021	0.795 $\pm$0.035	0.465 $\pm$0.096
β	0.034 $\pm$0.022	0.050 $\pm$0.006	0.079 $\pm$0.006	0.068 $\pm$0.006	0.037 $\pm$0.022
γ	12.540 $\pm$6.899	9.645 $\pm$0.870	3.069 $\pm$0.118	1.295 $\pm$0.036	1.153 $\pm$0.191
δ	2.500 $\pm$0.301	1.819 $\pm$0.063	1.614 $\pm$0.080	0.941 $\pm$0.083	0.295 $\pm$0.065
λ	0.161 $\pm$0.086	0.165 $\pm$0.015	0.330 $\pm$0.013	0.527 $\pm$0.012	0.662 $\pm$0.013
χ^2/DOF	112.4/95	113.5/95	109.8/95	80.2/95	77.2/95

reaction	$\sqrt{s}$ (GeV)	Radius (fm)		Reference
		Bowler	Gauss	
$pp \to pp\ 2\pi^+2\pi^-$	7.21	3.11 ± 10.9 1.07 ± 0.35	1.16 ± 0.63 0.97 ± 0.15	E766
$pp \to pp\ 3\pi^+3\pi^-$	7.21	0.80 ± 0.06 0.88 ± 0.05	0.93 ± 0.04 0.97 ± 0.04	E766
$pp \to pp\ 4\pi^+4\pi^-$	7.21	0.80 ± 0.03 0.70 ± 0.03	0.98 ± 0.03 0.88 ± 0.02	E766
$pp \to pp\ 5\pi^+5\pi^-$	7.21	0.77 ± 0.04 0.75 ± 0.03	1.01 ± 0.03 0.99 ± 0.03	E766
$pp \to pp\ 6\pi^+6\pi^-$	7.21	1.05 ± 0.68 1.02 ± 0.30	1.41 ± 0.41 1.29 ± 0.19	E766
K^+p & π^+p	22	-	0.8 ± 0.02	20
pp	26	-	1.02 ± 0.2	24
pp	27.4	-	1.2 ± 0.03	25
e^+e^-	29	-	0.65 ± 0.04	26
pp	31	-	~0.85	23

Reaction	n_π	$\Delta\eta$	**dn/dη**	$R_G^{(++)}$	$R_G^{(--)}$
$pp2\pi^+2\pi^-$	4	2.6	1.5	1.16 ± 0.63	0.97 ± 0.15
$pp3\pi^+3\pi^-$	6	2.5	2.5	0.93 ± 0.04	0.97 ± 0.04
$pp4\pi^+4\pi^-$	8	3.6	3.6	0.98 ± 0.03	0.88 ± 0.02
$pp5\pi^+5\pi^-$	10	1.8	5.6	1.01 ± 0.03	0.99 ± 0.03
$pp6\pi^+6\pi^-$	12	1.6	7.5	1.41 ± 0.41	1.29 ± 0.19

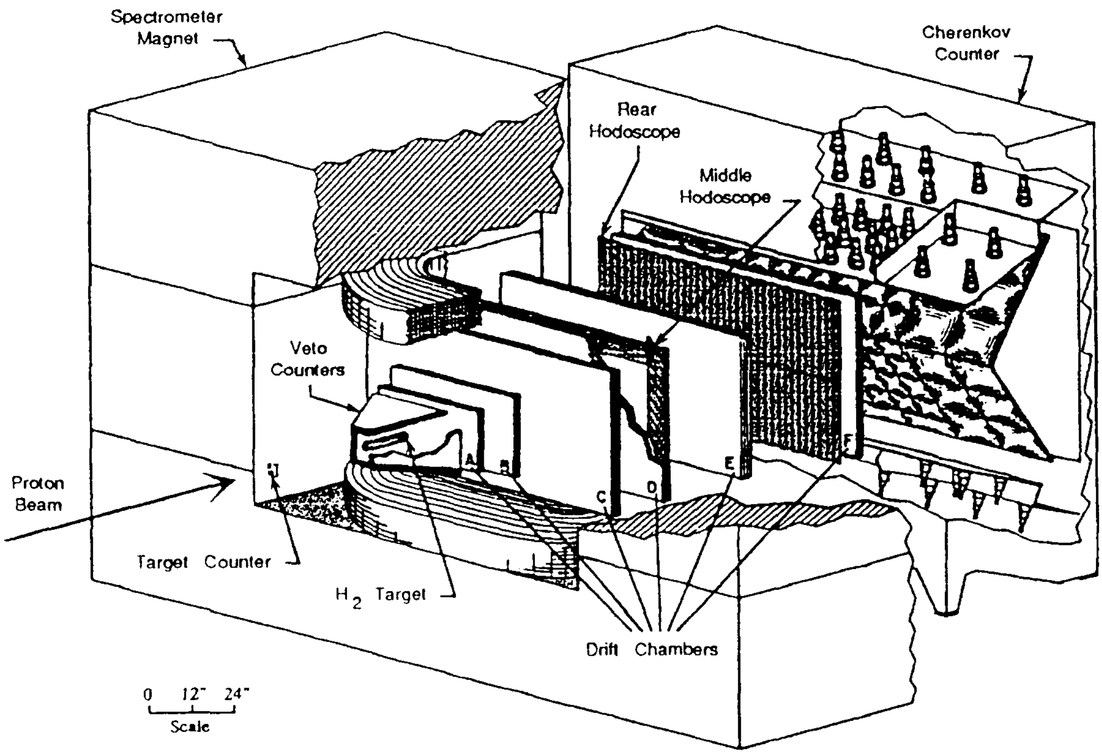
Spectrometer
Magnet
Cherenkov
Counter
Rear
Hodoscope
Middle
Hodoscope
Veto
Counters
Proton
Beam
Target Counter
H2 Target
Drift Chambers
A
B
C
D
E
F
0 12" 24"
Scale

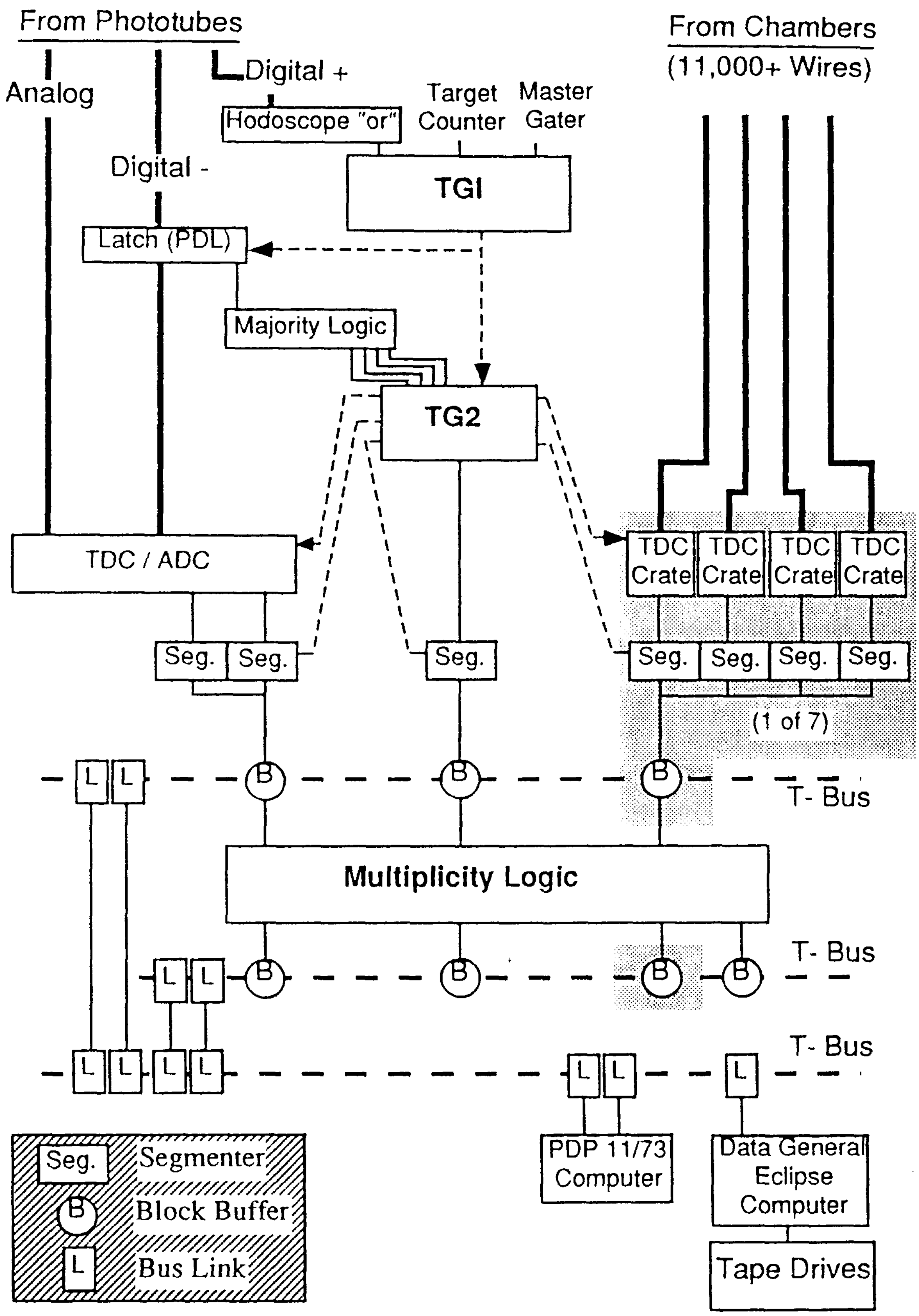

From Phototubes
Analog
Digital -
Digital +
Hodoscope "or"
Target Counter
Master Gater
TGI
Latch (PDL)
Majority Logic
TG2
From Chambers
(11,000+ Wires)
TDC / ADC
TDC Crate
TDC Crate
TDC Crate
TDC Crate
Seg.
Seg.
Seg.
Seg.
Seg.
Seg.
Seg.
(1 of 7)
B
L
T- Bus
Multiplicity Logic
T- Bus
T- Bus
PDP 11/73 Computer
Data General Eclipse Computer
Tape Drives
Seg. Segmenter
B Block Buffer
L Bus Link

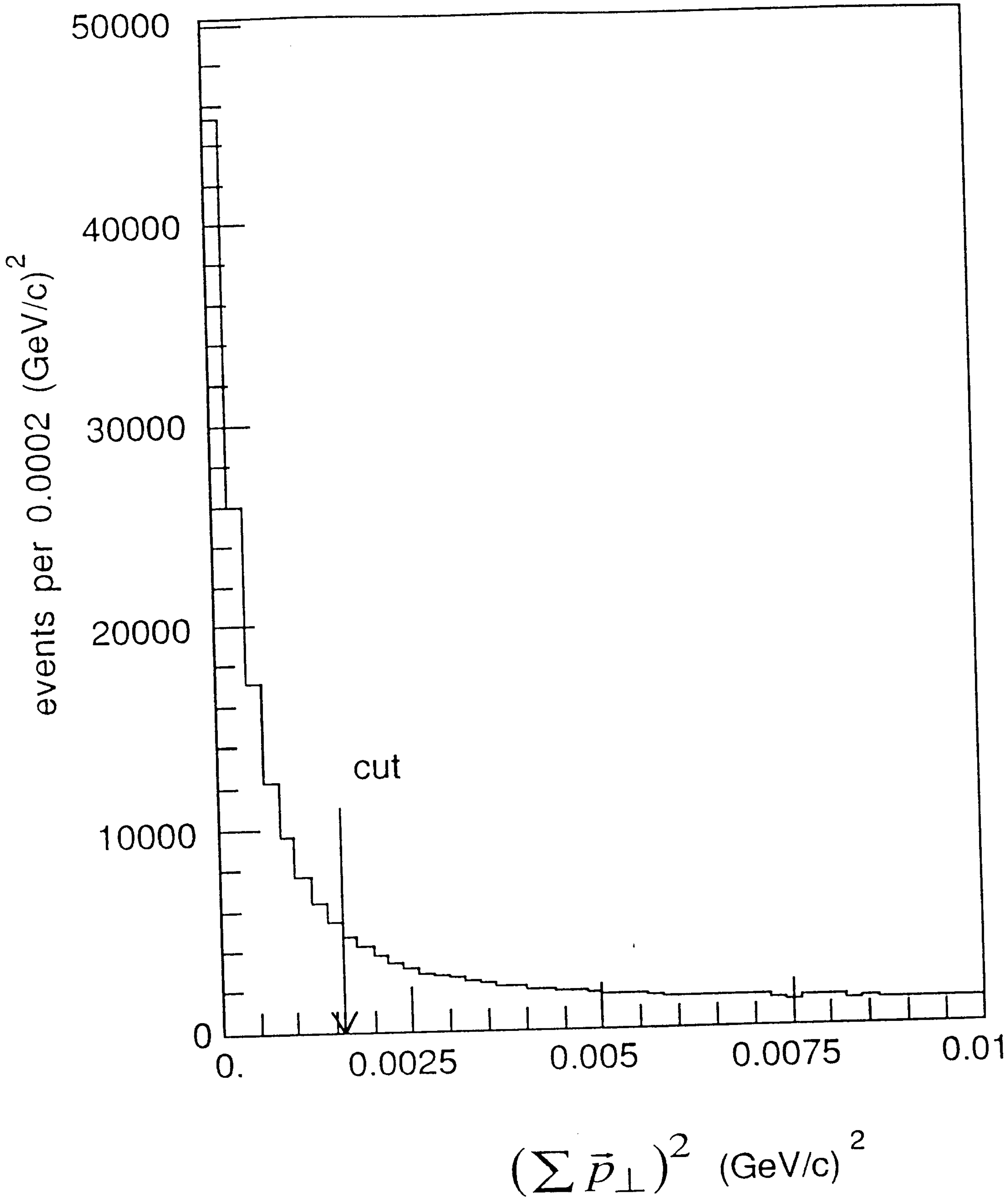

50000
40000
30000
20000
10000
0
events per 0.0002 (GeV/c)^2
cut
0.
0.0025
0.005
0.0075
0.01
$(\sum \vec{p}_\perp)^2$ (GeV/c)^2

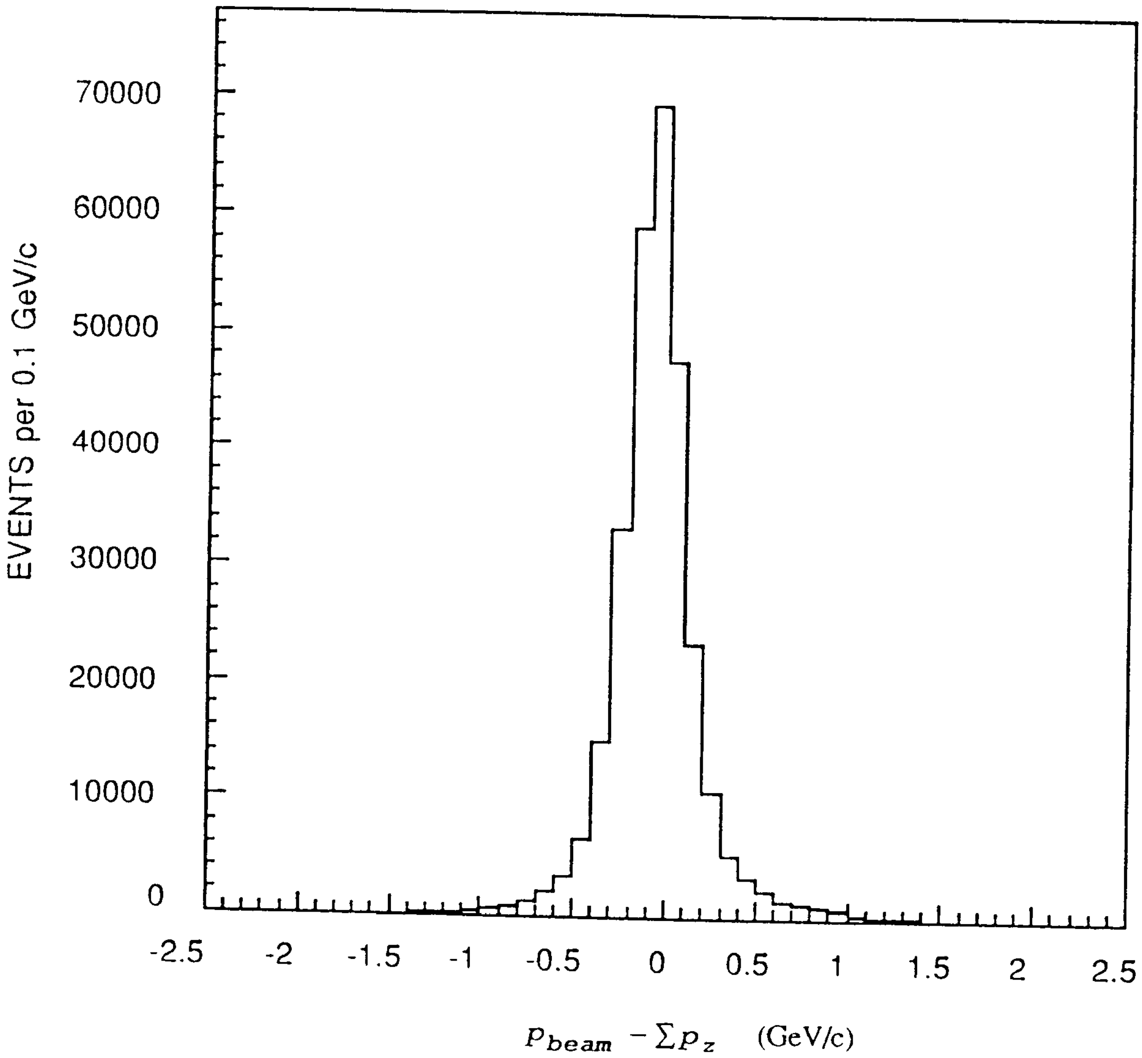

EVENTS per 0.1 GeV/c
70000
60000
50000
40000
30000
20000
10000
0
-2.5
-2
-1.5
-1
-0.5
0
0.5
1
1.5
2
2.5
$p_{beam} - \sum p_z$ (GeV/c)

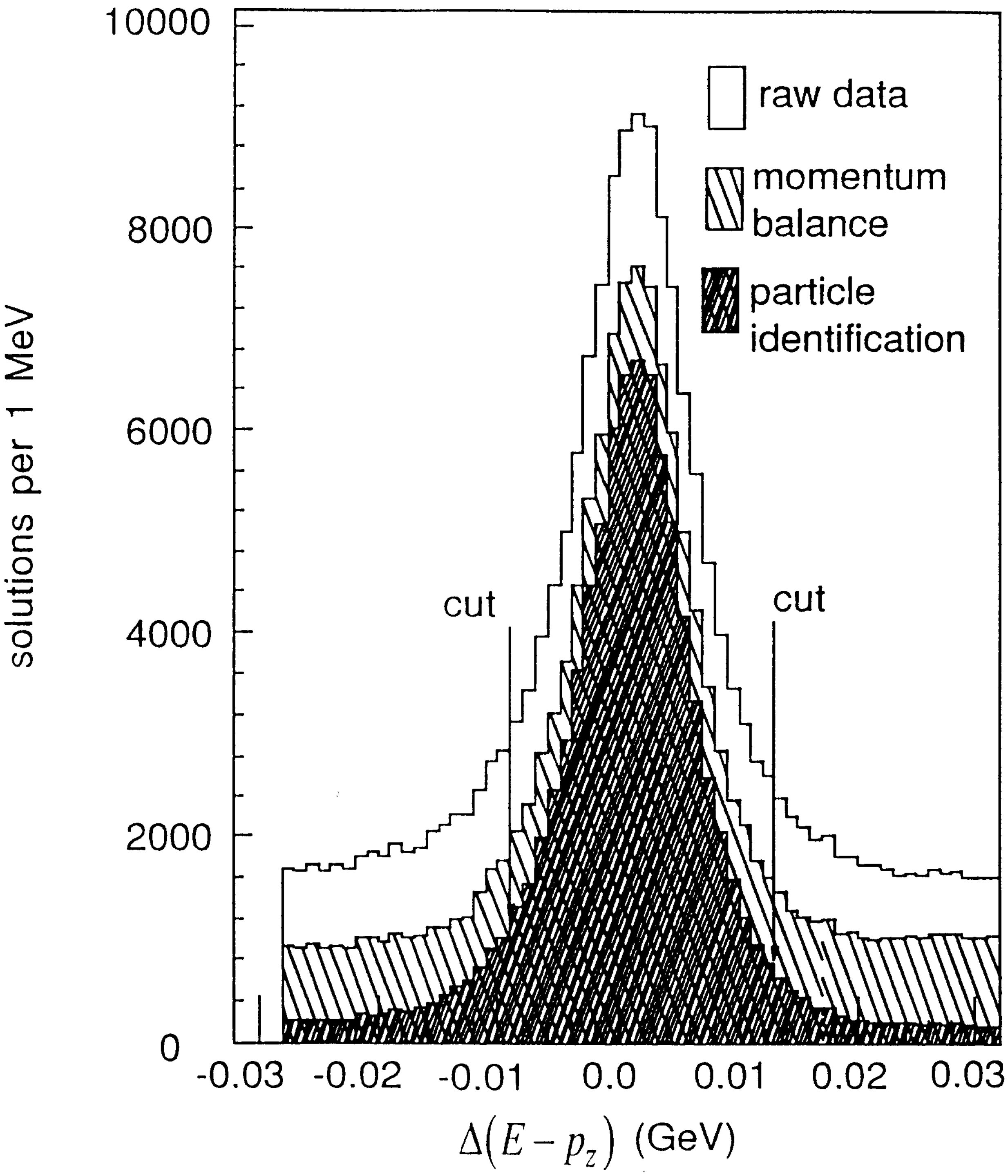

10000
8000
6000
4000
2000
0
solutions per 1 MeV
raw data
momentum balance
particle identification
cut
cut
-0.03
-0.02
-0.01
0.0
0.01
0.02
0.03
Δ(E − p_z) (GeV)

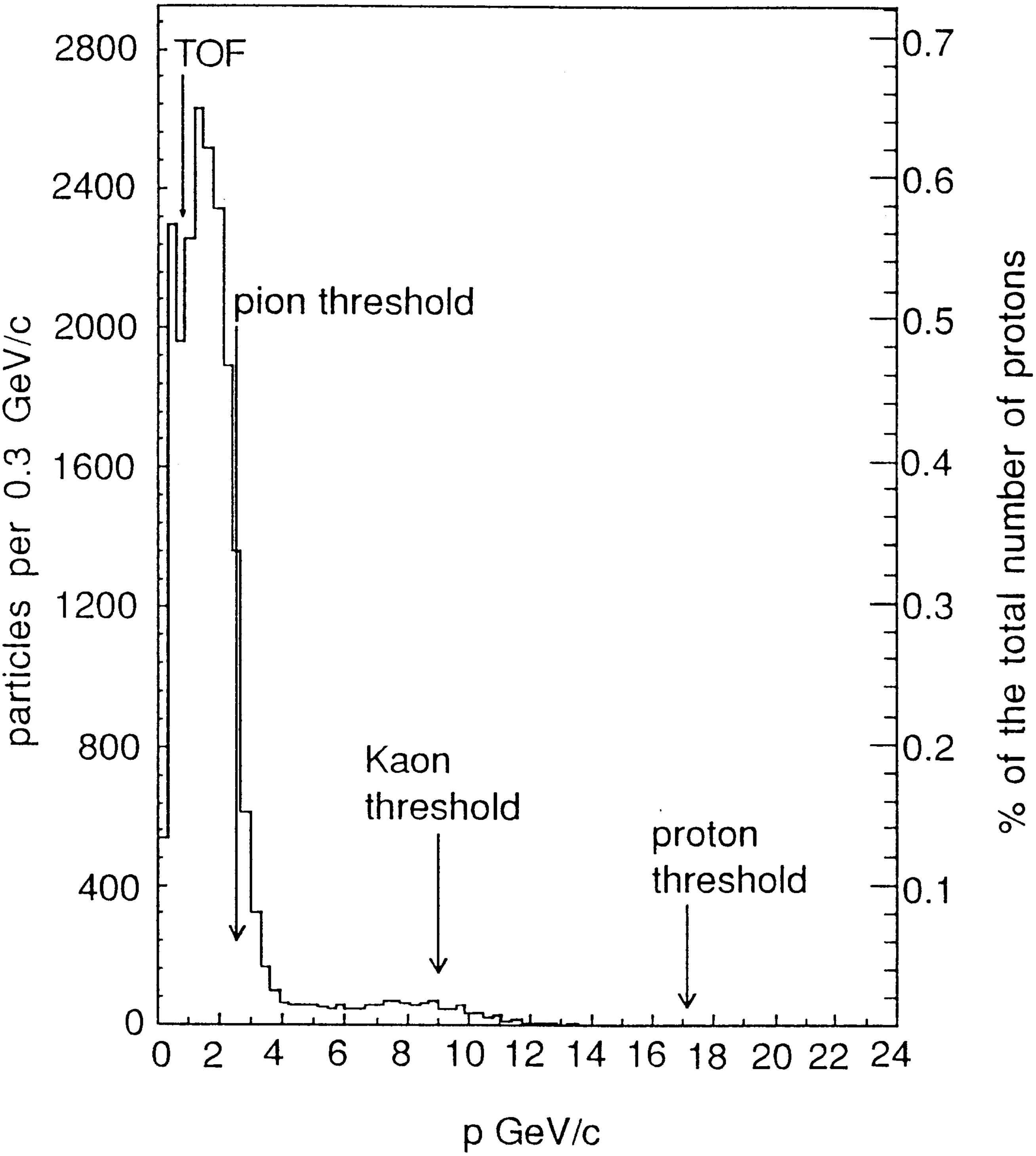

TOF
pion threshold
Kaon threshold
proton threshold
particles per 0.3 GeV/c
% of the total number of protons
p GeV/c
0
400
800
1200
1600
2000
2400
2800
0.1
0.2
0.3
0.4
0.5
0.6
0.7
0 2 4 6 8 10 12 14 16 18 20 22 24

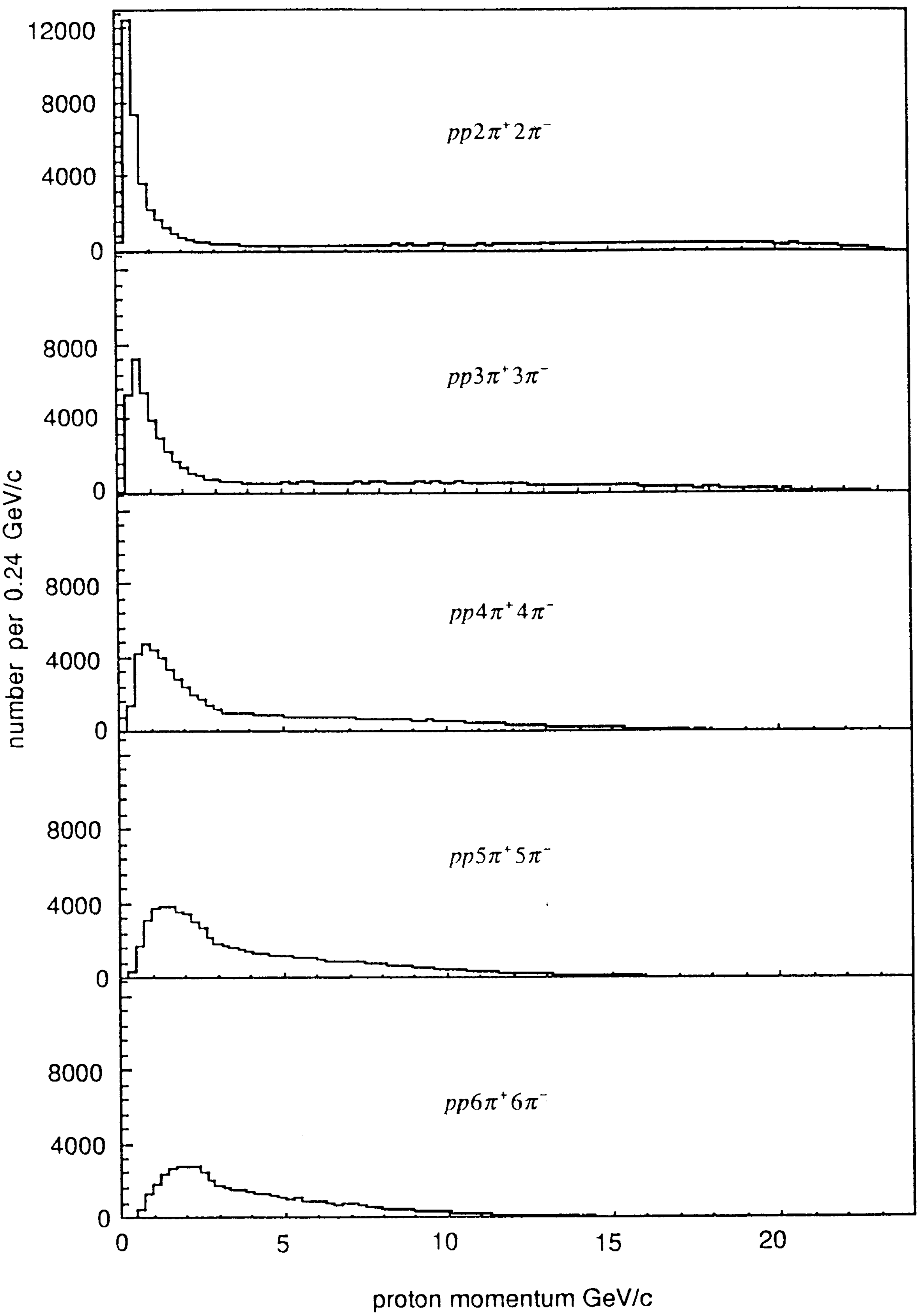

12000
8000
4000
0
$pp2\pi^+2\pi^-$
8000
4000
0
$pp3\pi^+3\pi^-$
8000
4000
0
$pp4\pi^+4\pi^-$
8000
4000
0
$pp5\pi^+5\pi^-$
8000
4000
0
$pp6\pi^+6\pi^-$
number per 0.24 GeV/c
0
5
10
15
20
proton momentum GeV/c

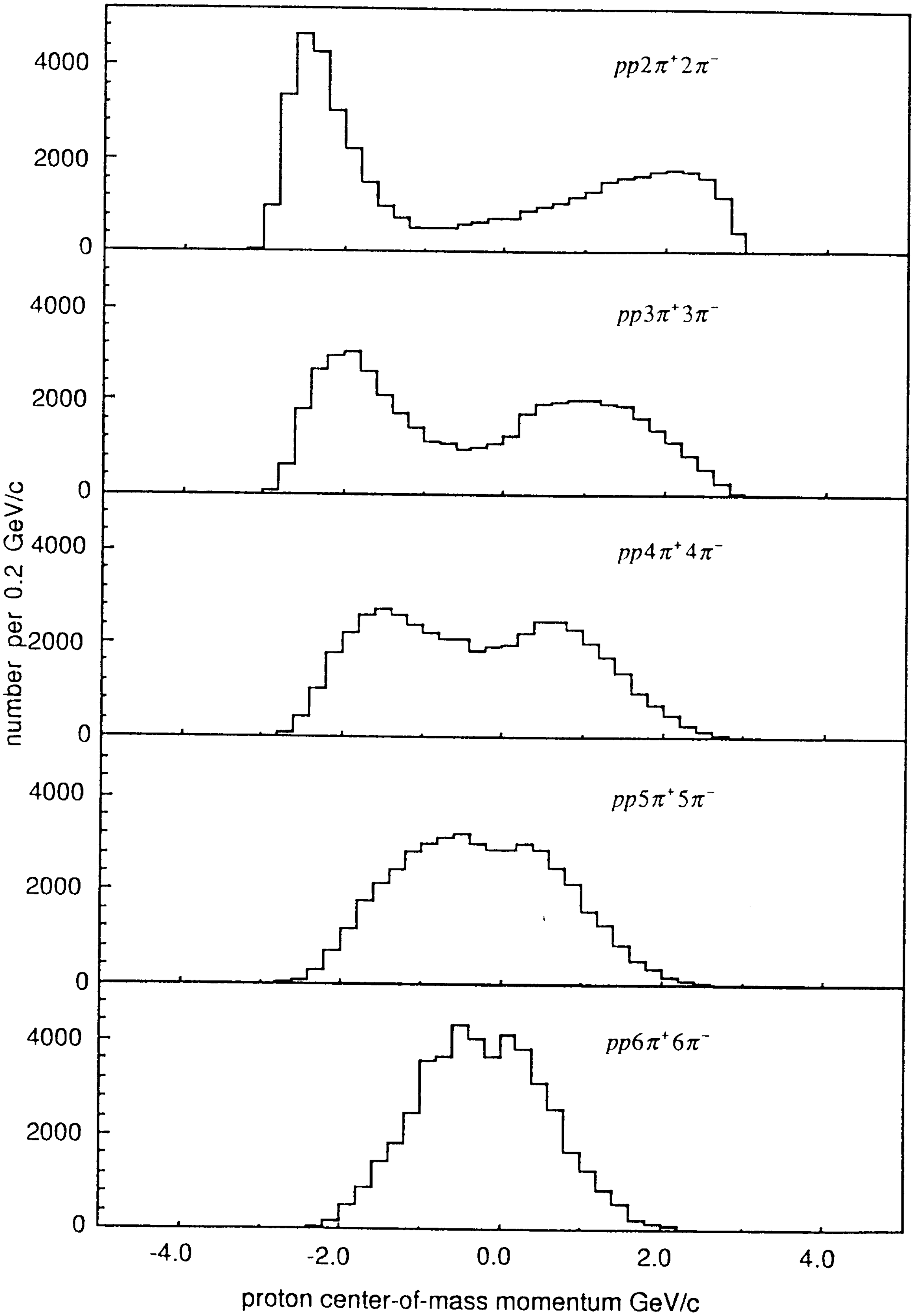

number per 0.2 GeV/c
4000
2000
0
$pp2\pi^+2\pi^-$
$pp3\pi^+3\pi^-$
$pp4\pi^+4\pi^-$
$pp5\pi^+5\pi^-$
$pp6\pi^+6\pi^-$
-4.0
-2.0
0.0
2.0
4.0
proton center-of-mass momentum GeV/c

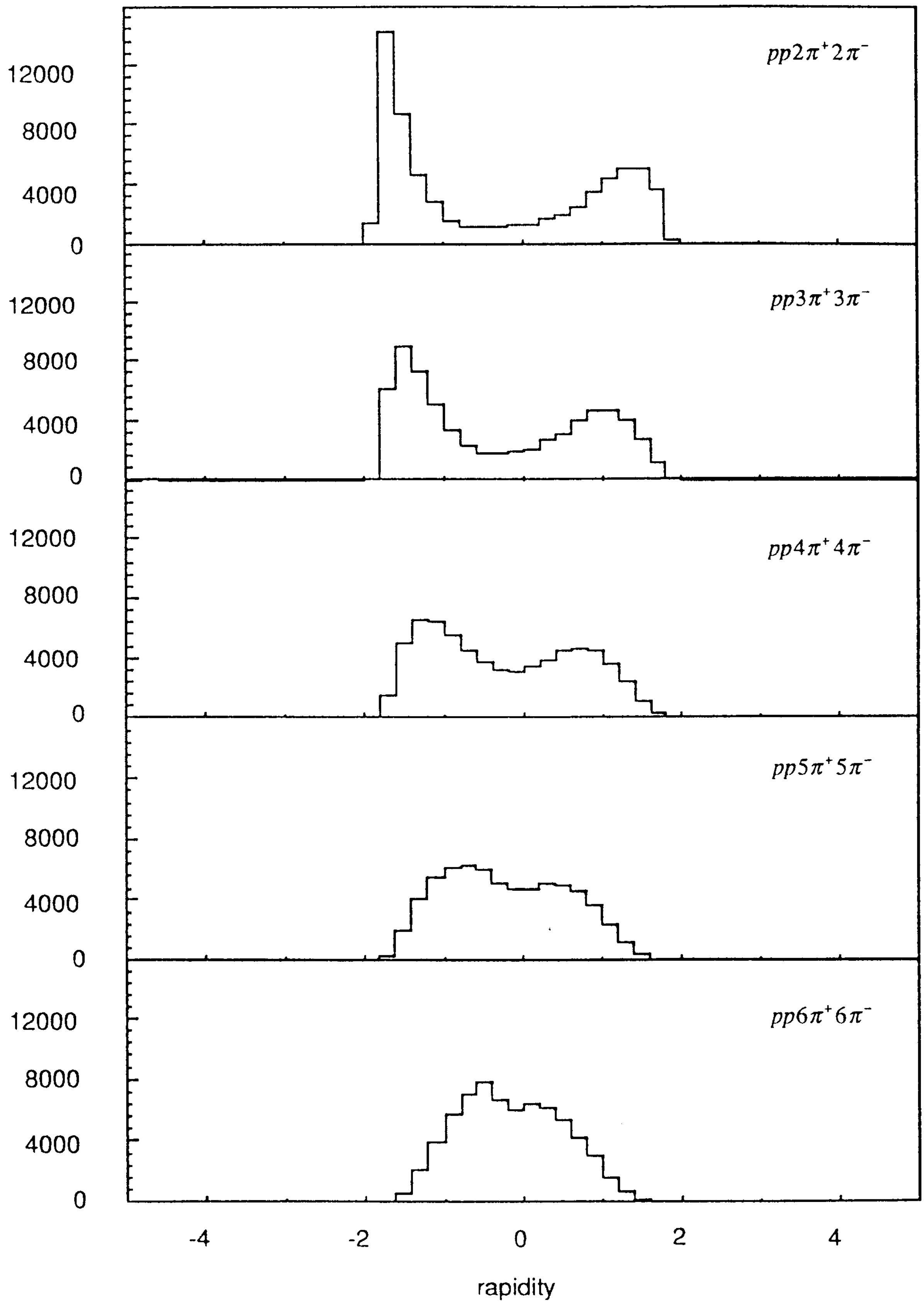

$pp2\pi^+2\pi^-$
$pp3\pi^+3\pi^-$
$pp4\pi^+4\pi^-$
$pp5\pi^+5\pi^-$
$pp6\pi^+6\pi^-$
12000
8000
4000
0
-4
-2
0
2
4
rapidity

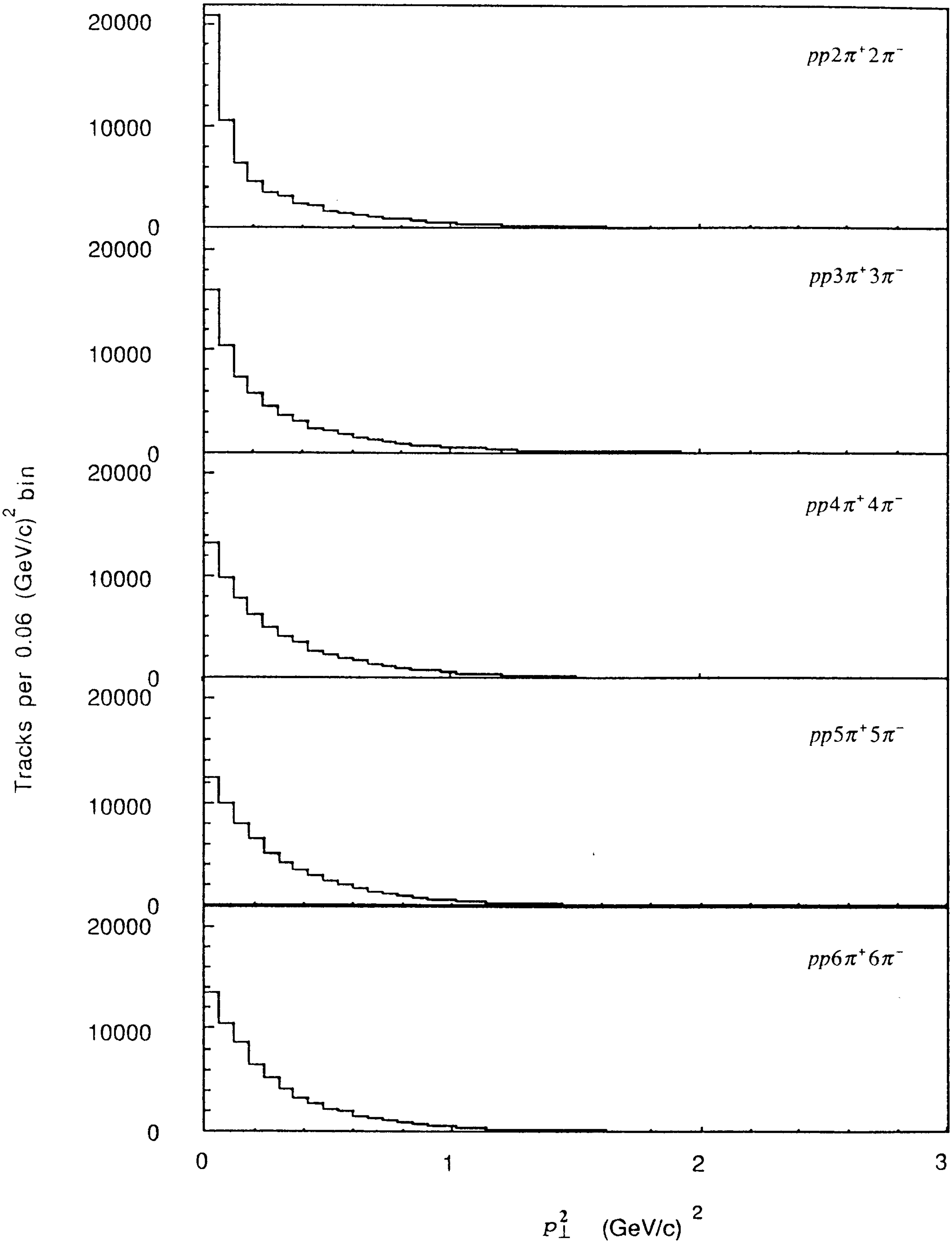

Tracks per 0.06 (GeV/c)^2 bin
20000
10000
0
$pp2\pi^+2\pi^-$
$pp3\pi^+3\pi^-$
$pp4\pi^+4\pi^-$
$pp5\pi^+5\pi^-$
$pp6\pi^+6\pi^-$
0
1
2
3
$p_\perp^2$ (GeV/c)^2

Proton center of mass $P_{longitudinal}$ V.S. $P_{transverse}$

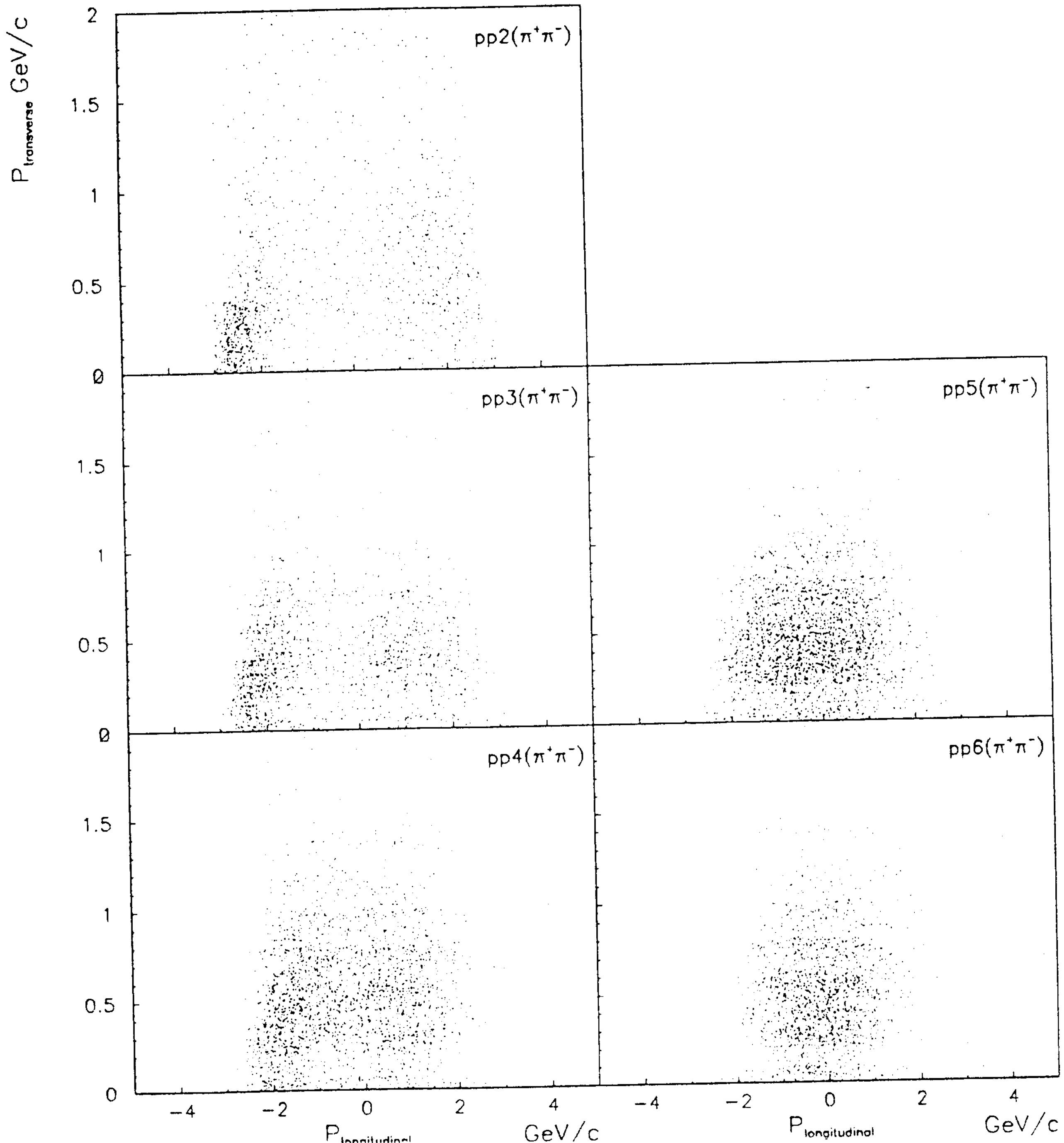

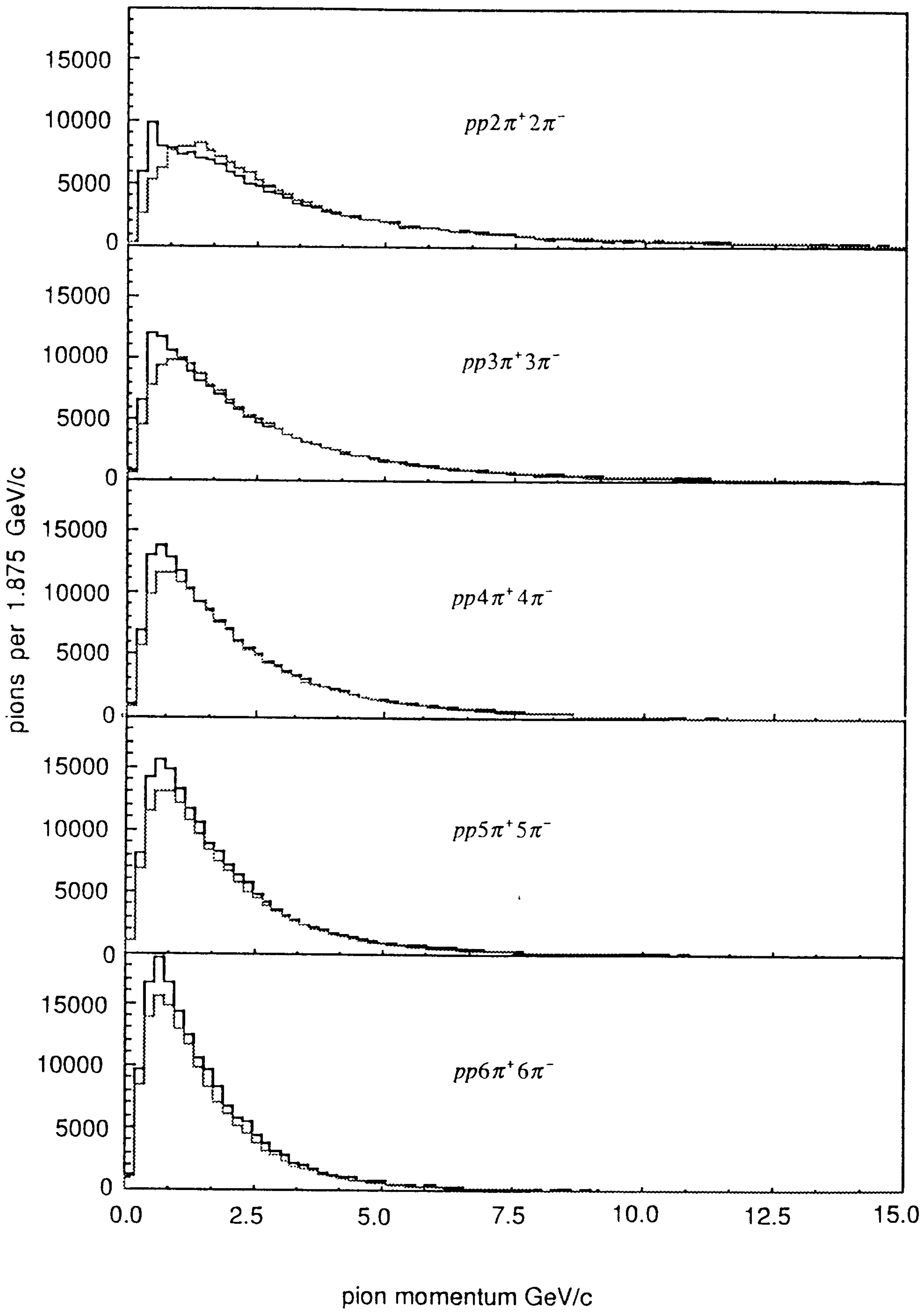

pions per 1.875 GeV/c
pion momentum GeV/c
$pp2\pi^+2\pi^-$
$pp3\pi^+3\pi^-$
$pp4\pi^+4\pi^-$
$pp5\pi^+5\pi^-$
$pp6\pi^+6\pi^-$
0
5000
10000
15000
0.0
2.5
5.0
7.5
10.0
12.5
15.0

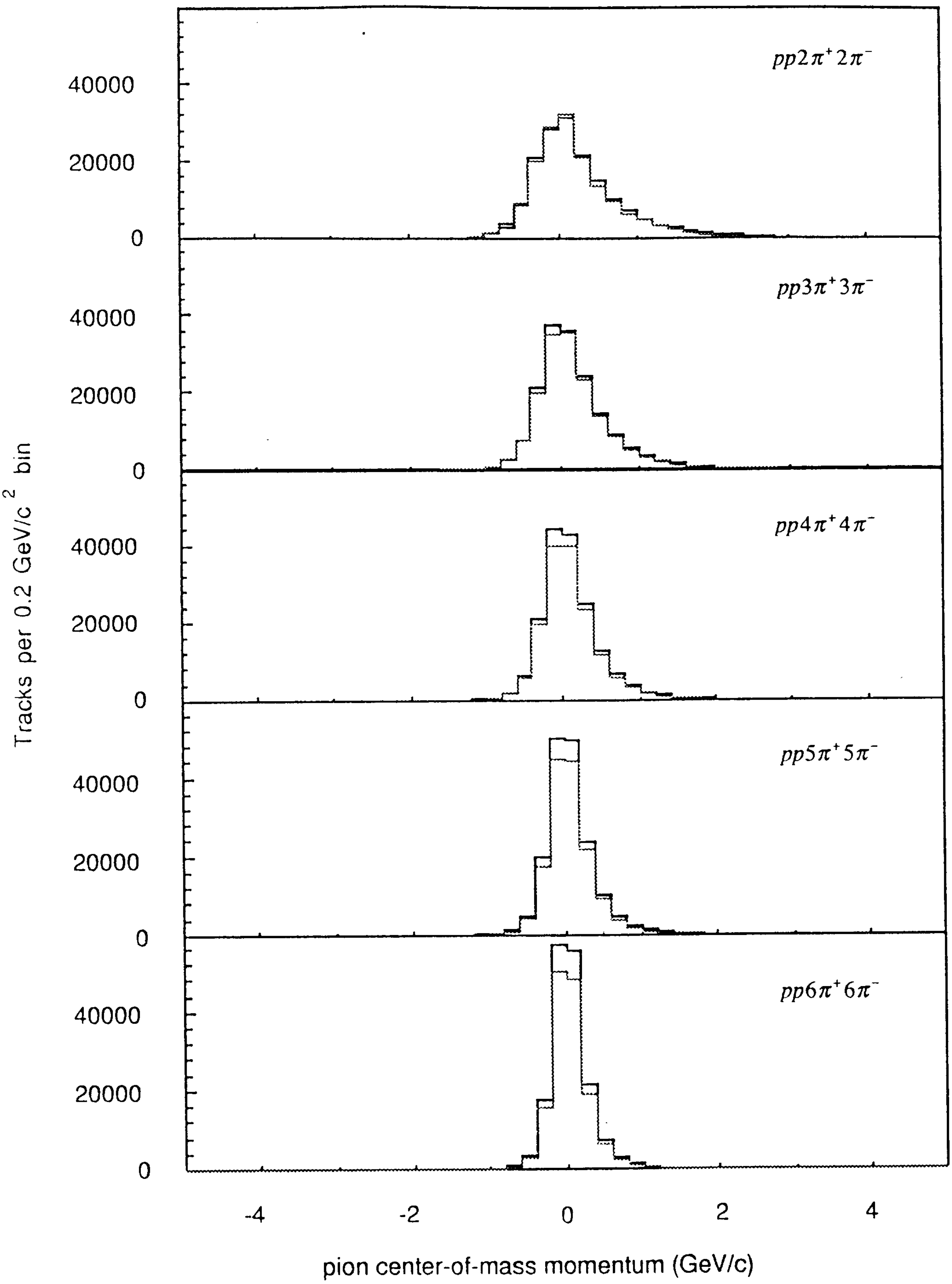

$pp2\pi^+2\pi^-$
$pp3\pi^+3\pi^-$
$pp4\pi^+4\pi^-$
$pp5\pi^+5\pi^-$
$pp6\pi^+6\pi^-$
40000
20000
0
Tracks per 0.2 GeV/c^2 bin
-4
-2
0
2
4
pion center-of-mass momentum (GeV/c)

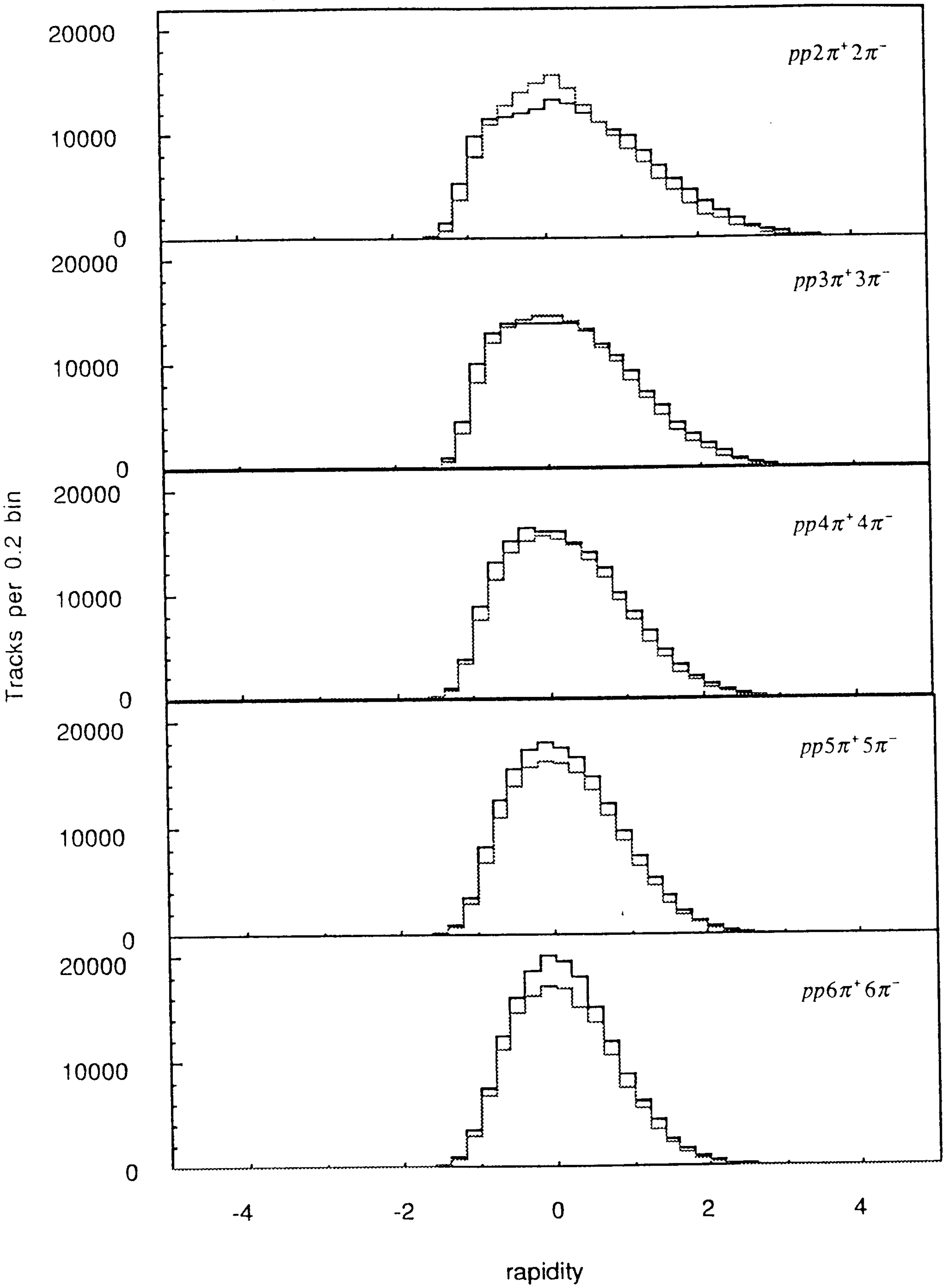

$pp2\pi^+2\pi^-$
$pp3\pi^+3\pi^-$
$pp4\pi^+4\pi^-$
$pp5\pi^+5\pi^-$
$pp6\pi^+6\pi^-$
Tracks per 0.2 bin
20000
10000
0
-4
-2
0
2
4
rapidity

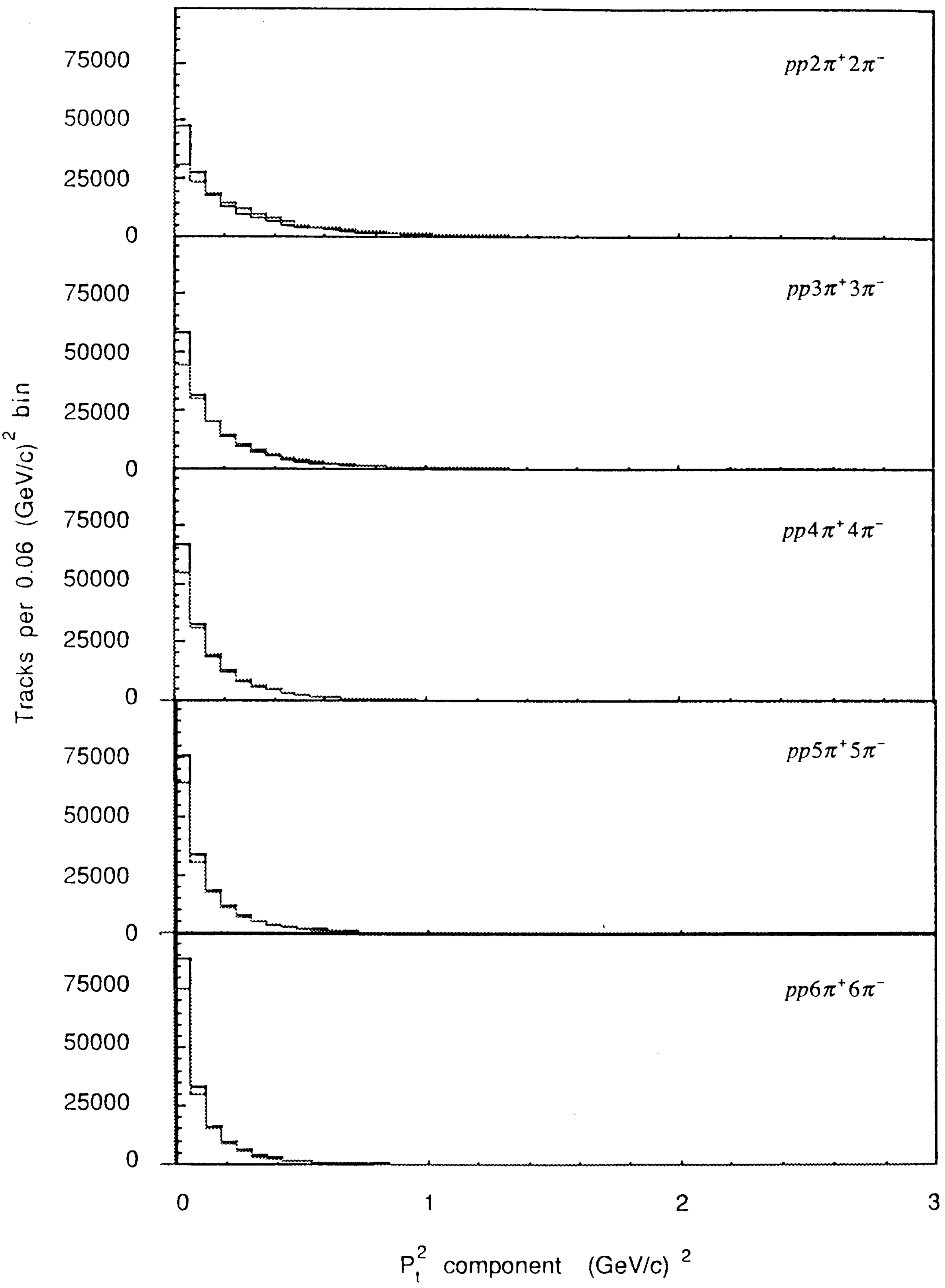

$pp2\pi^+2\pi^-$
$pp3\pi^+3\pi^-$
$pp4\pi^+4\pi^-$
$pp5\pi^+5\pi^-$
$pp6\pi^+6\pi^-$
75000
50000
25000
0
0
1
2
3
Tracks per 0.06 $(GeV/c)^2$ bin
P_t^2 component $(GeV/c)^2$

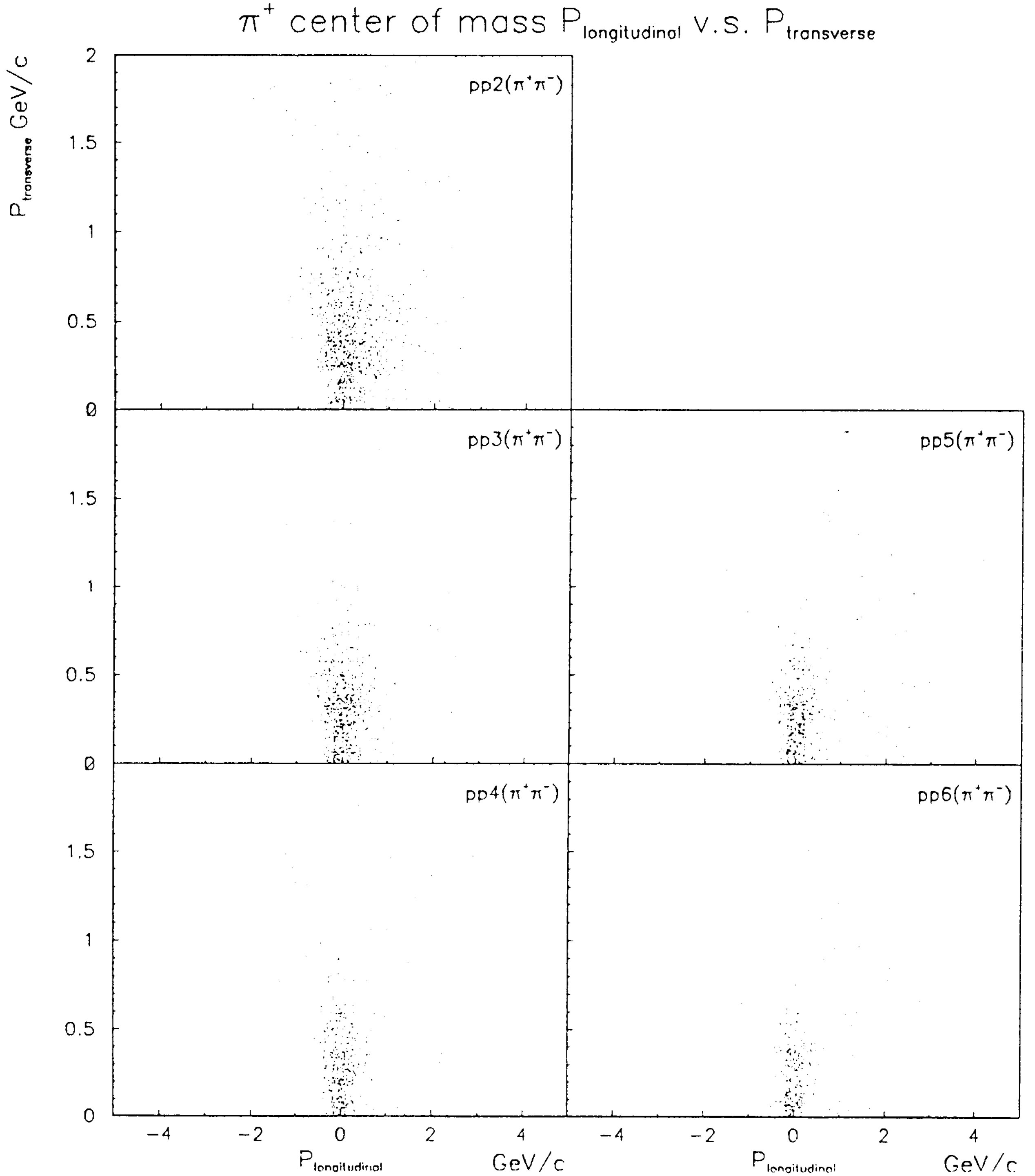

π+ center of mass P longitudinal V.S. P transverse
P transverse GeV/c
pp2(π+π-)
pp3(π+π-)
pp4(π+π-)
pp5(π+π-)
pp6(π+π-)
P longitudinal GeV/c
P longitudinal GeV/c

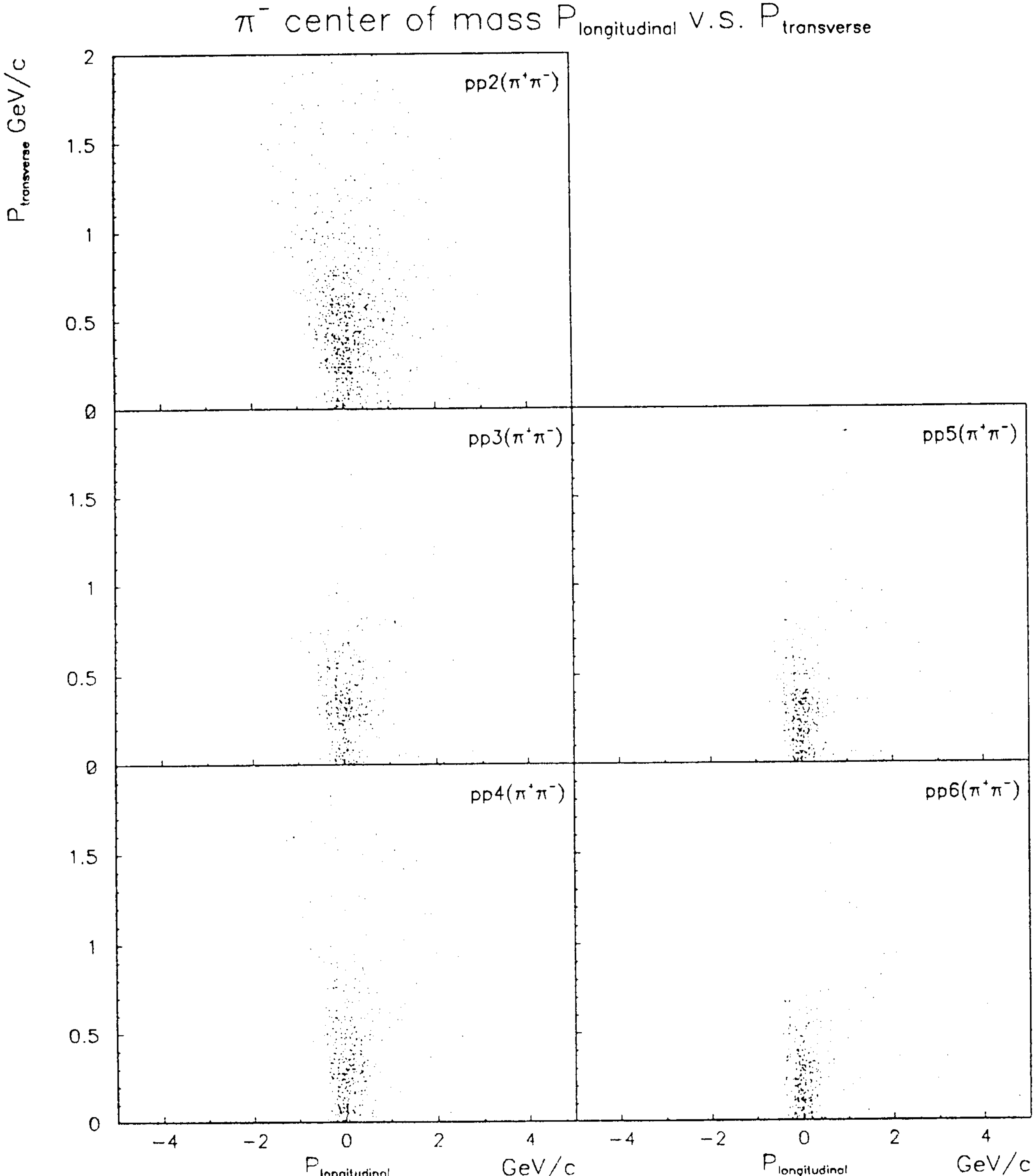

π⁻ center of mass P longitudinal V.S. P transverse
P transverse GeV/c
pp2(π⁺π⁻)
pp3(π⁺π⁻)
pp4(π⁺π⁻)
pp5(π⁺π⁻)
pp6(π⁺π⁻)
P longitudinal GeV/c

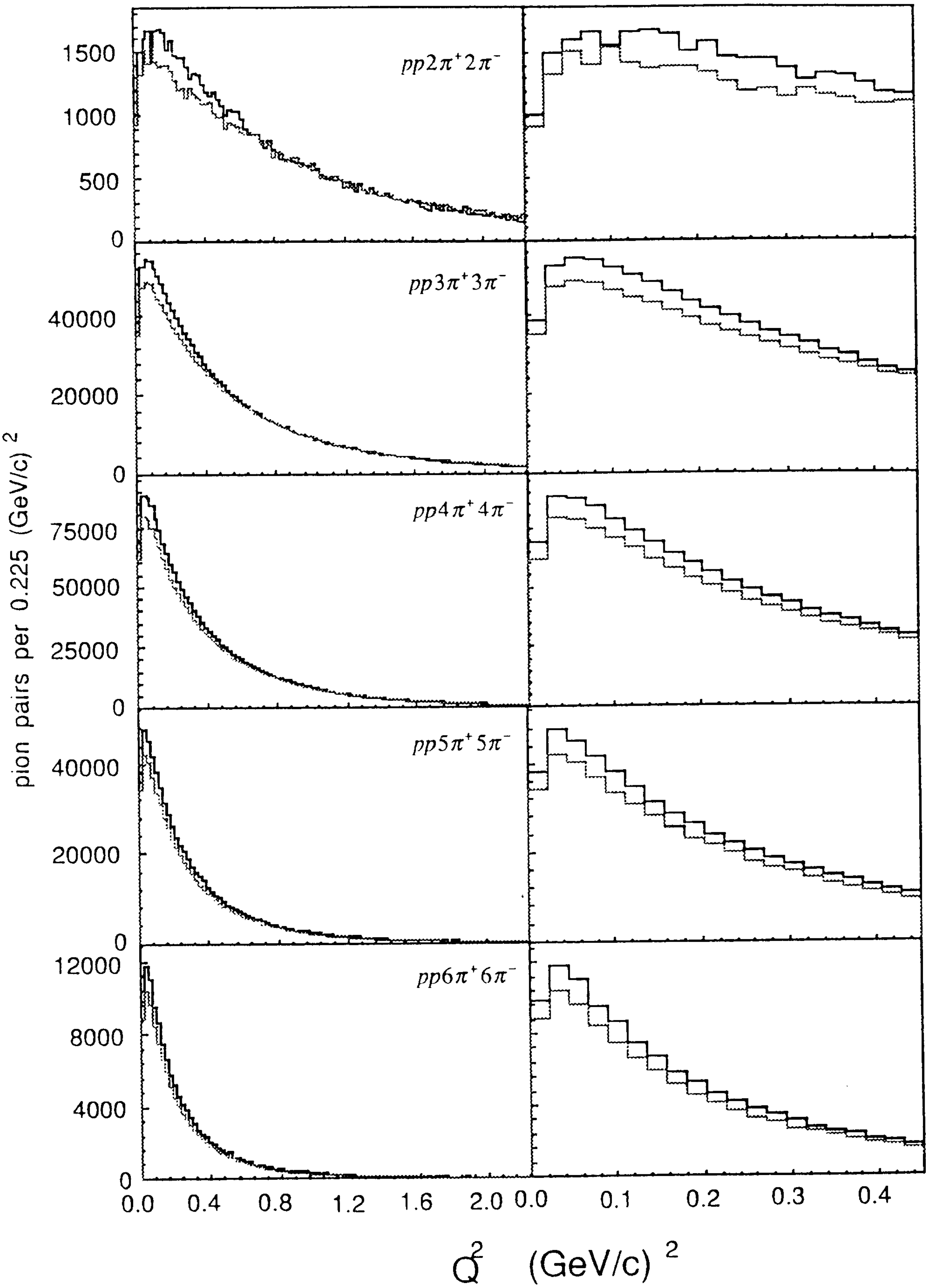

$pp2\pi^+2\pi^-$
$pp3\pi^+3\pi^-$
$pp4\pi^+4\pi^-$
$pp5\pi^+5\pi^-$
$pp6\pi^+6\pi^-$
pion pairs per 0.225 (GeV/c) 2
Q^2 (GeV/c) 2

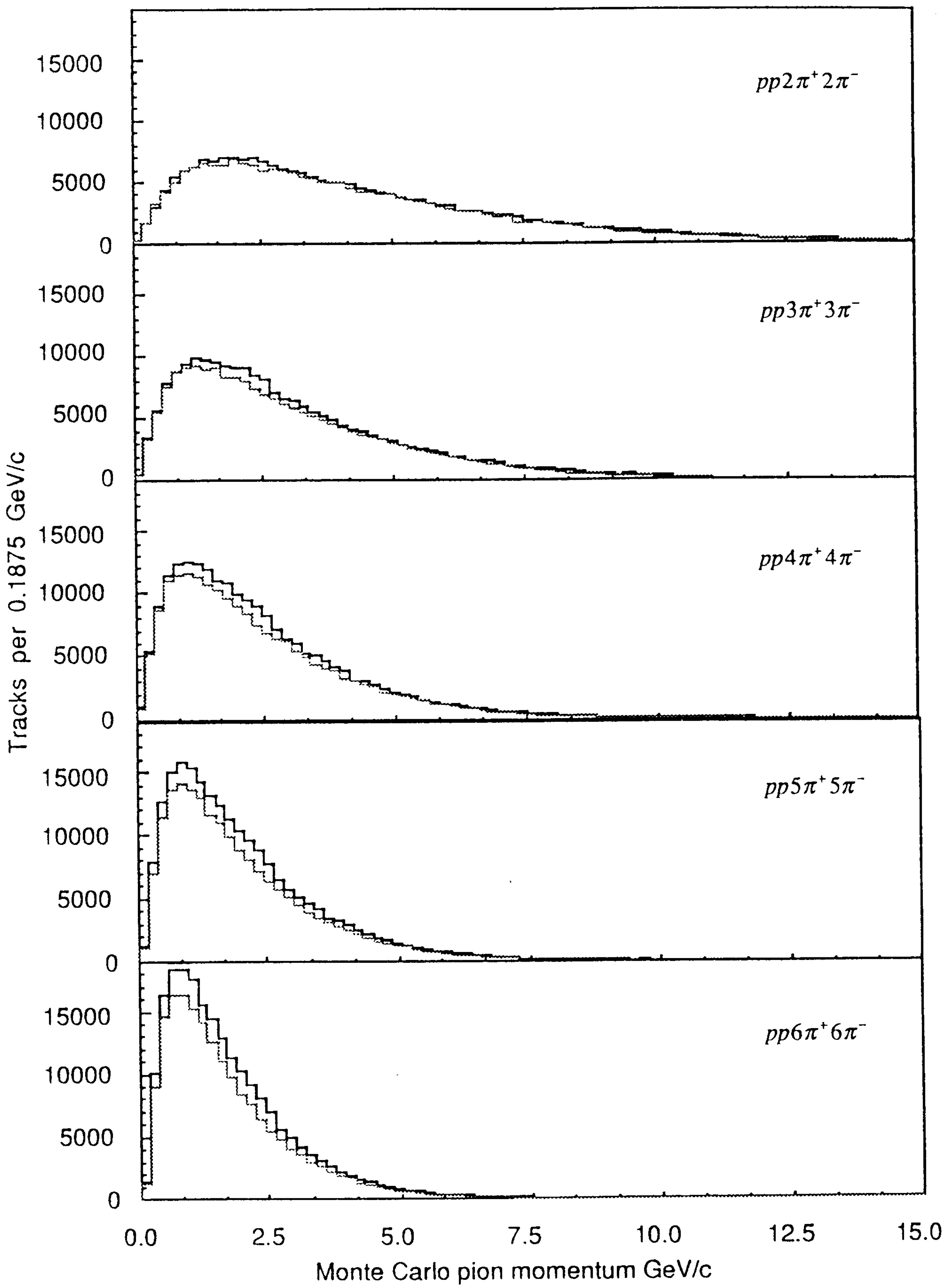

$pp2\pi^+2\pi^-$
$pp3\pi^+3\pi^-$
$pp4\pi^+4\pi^-$
$pp5\pi^+5\pi^-$
$pp6\pi^+6\pi^-$
Tracks per 0.1875 GeV/c
Monte Carlo pion momentum GeV/c
0
5000
10000
15000
0.0
2.5
5.0
7.5
10.0
12.5
15.0

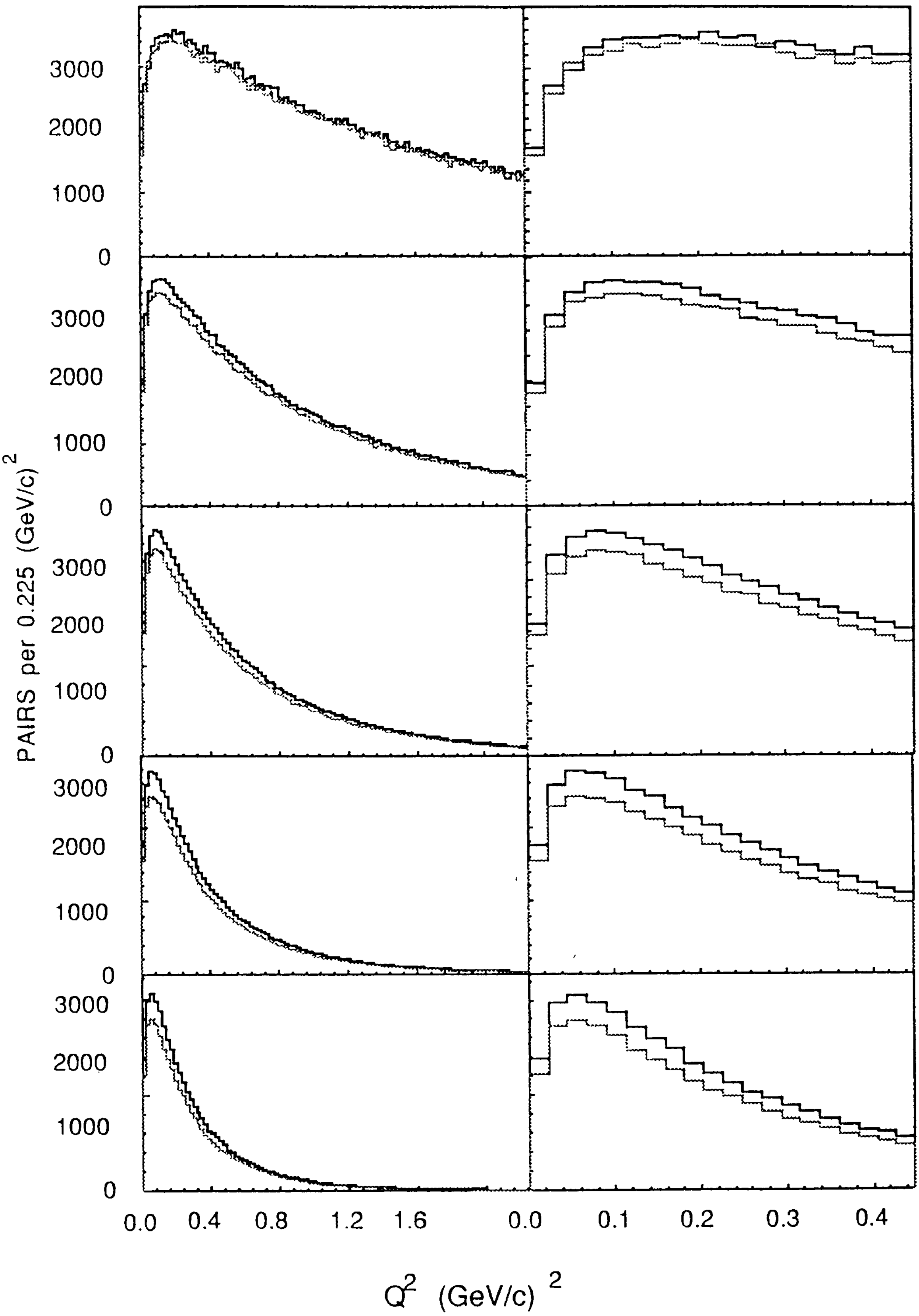

PAIRS per 0.225 (GeV/c)^2
0
1000
2000
3000
0.0
0.4
0.8
1.2
1.6
0.0
0.1
0.2
0.3
0.4
Q^2 (GeV/c)^2

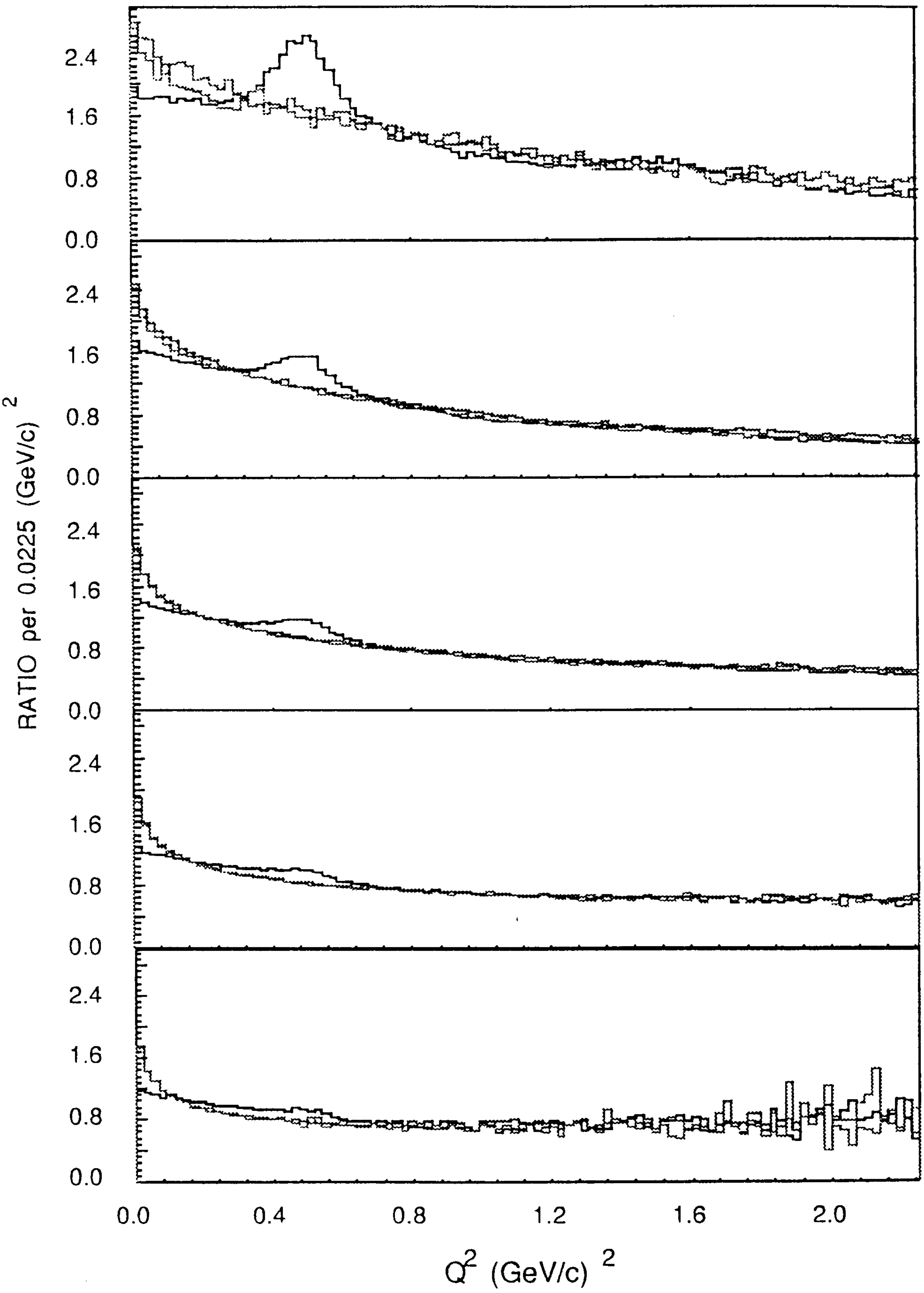
2.4
1.6
0.8
0.0
RATIO per 0.0225 (GeV/c)^2
0.0
0.4
0.8
1.2
1.6
2.0
Q^2 (GeV/c)^2

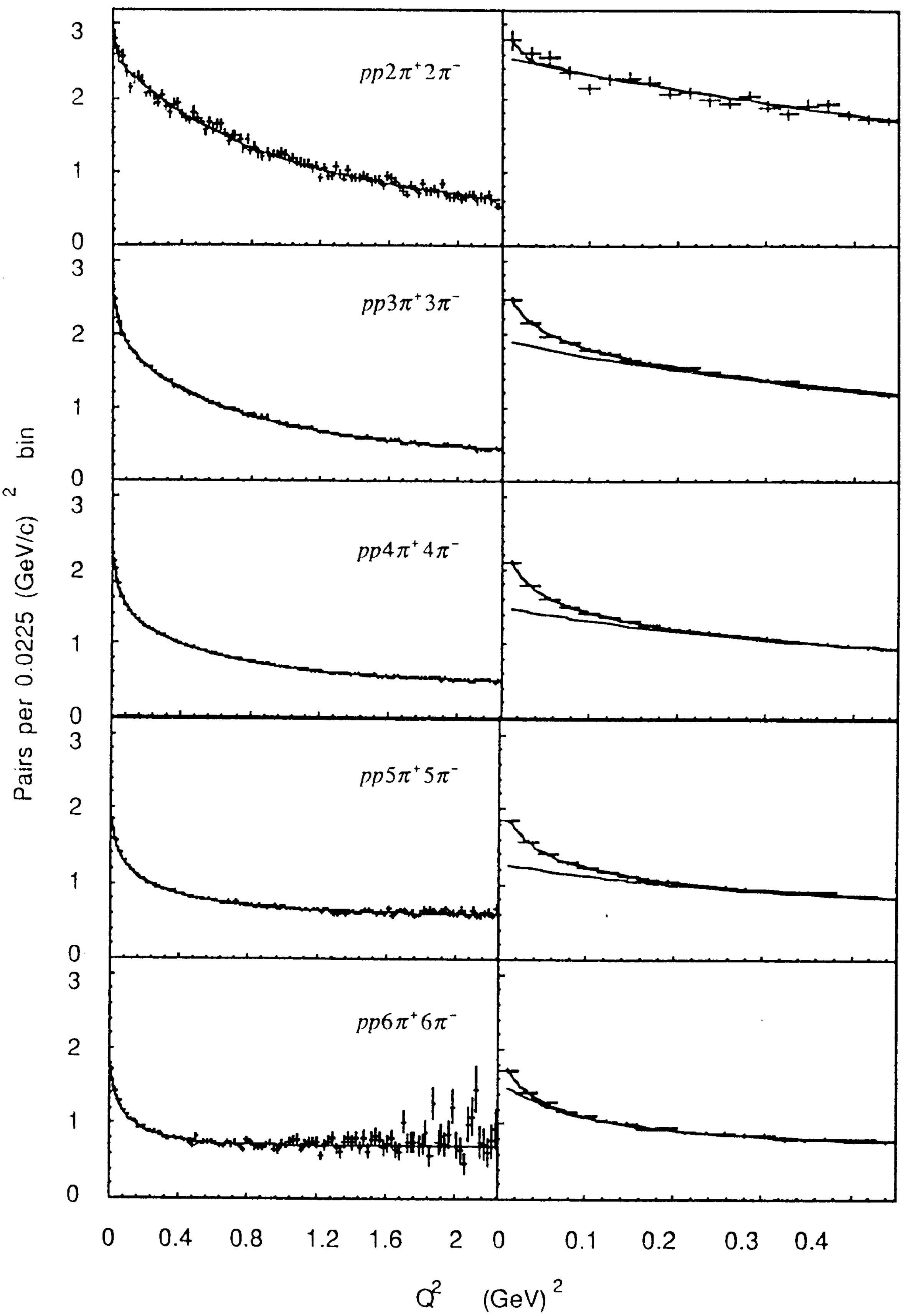

$pp2\pi^+2\pi^-$
$pp3\pi^+3\pi^-$
$pp4\pi^+4\pi^-$
$pp5\pi^+5\pi^-$
$pp6\pi^+6\pi^-$
Pairs per 0.0225 (GeV/c)^2 bin
0
1
2
3
0
0.4
0.8
1.2
1.6
2
0.1
0.2
0.3
0.4
Q^2 (GeV)^2

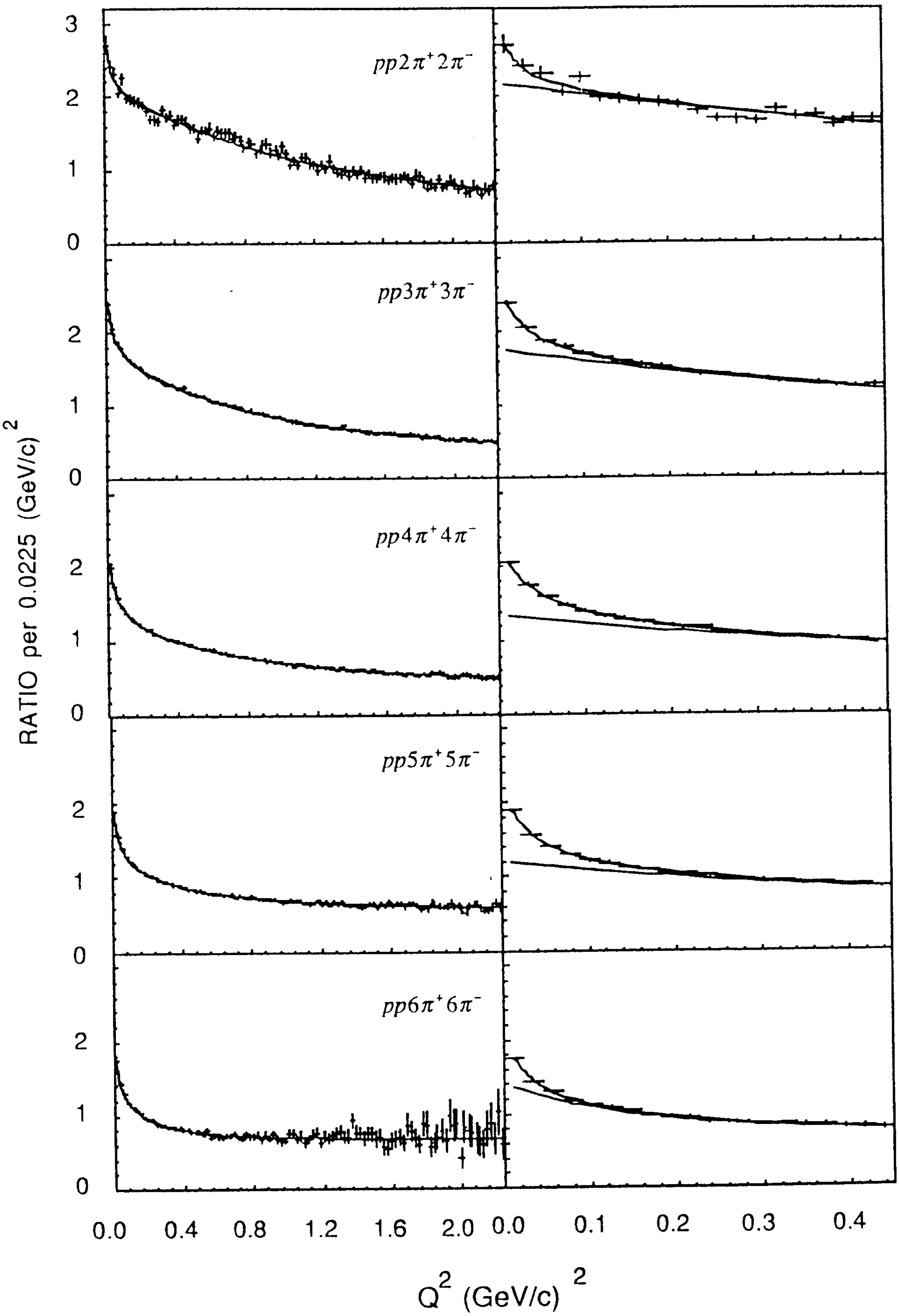

RATIO per 0.0225 (GeV/c)^2
$pp2\pi^+2\pi^-$
$pp3\pi^+3\pi^-$
$pp4\pi^+4\pi^-$
$pp5\pi^+5\pi^-$
$pp6\pi^+6\pi^-$
0.0 0.4 0.8 1.2 1.6 2.0
0.0 0.1 0.2 0.3 0.4
Q^2 (GeV/c)^2

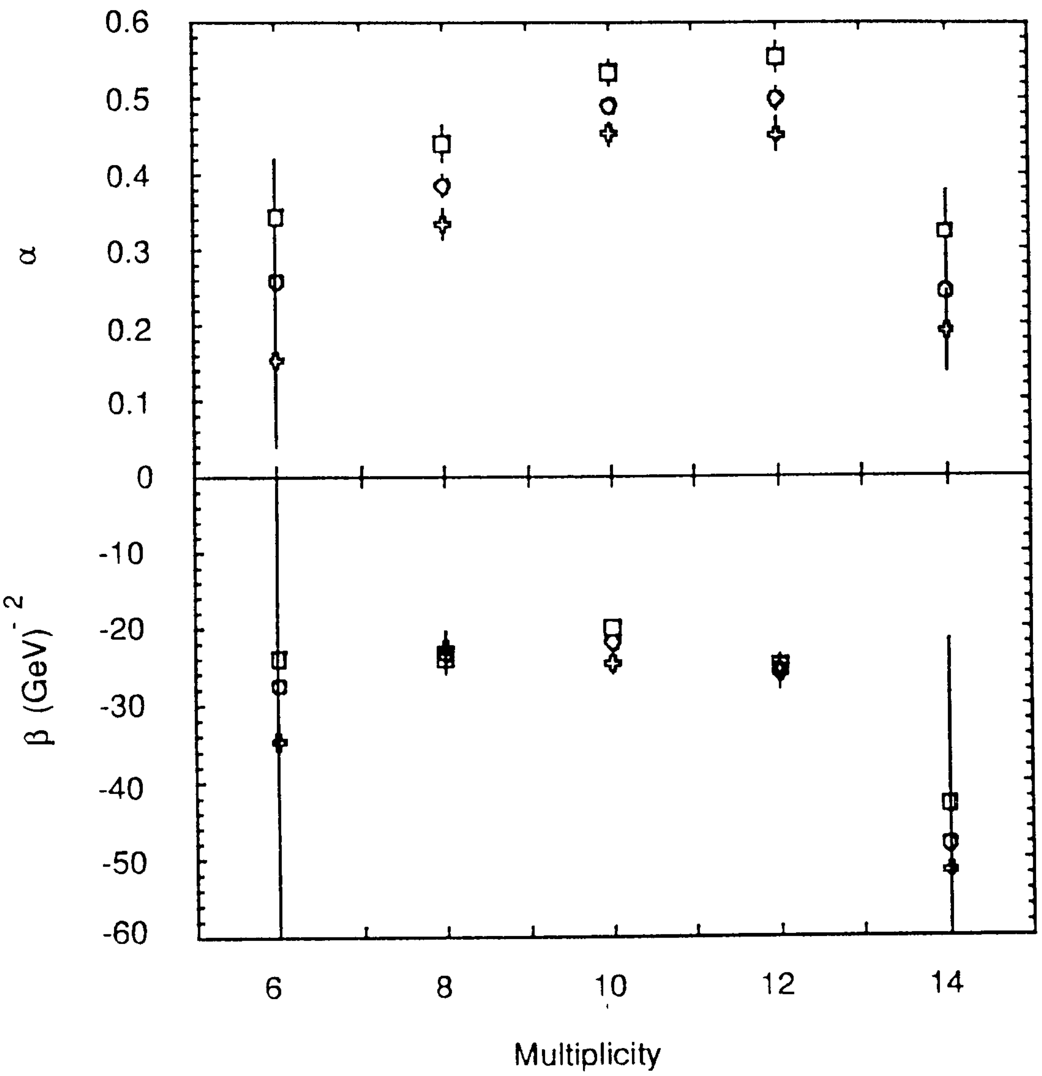
0.6
0.5
0.4
0.3
0.2
0.1
0
α
-10
-20
-30
-40
-50
-60
β (GeV)$^{-2}$
6
8
10
12
14
Multiplicity

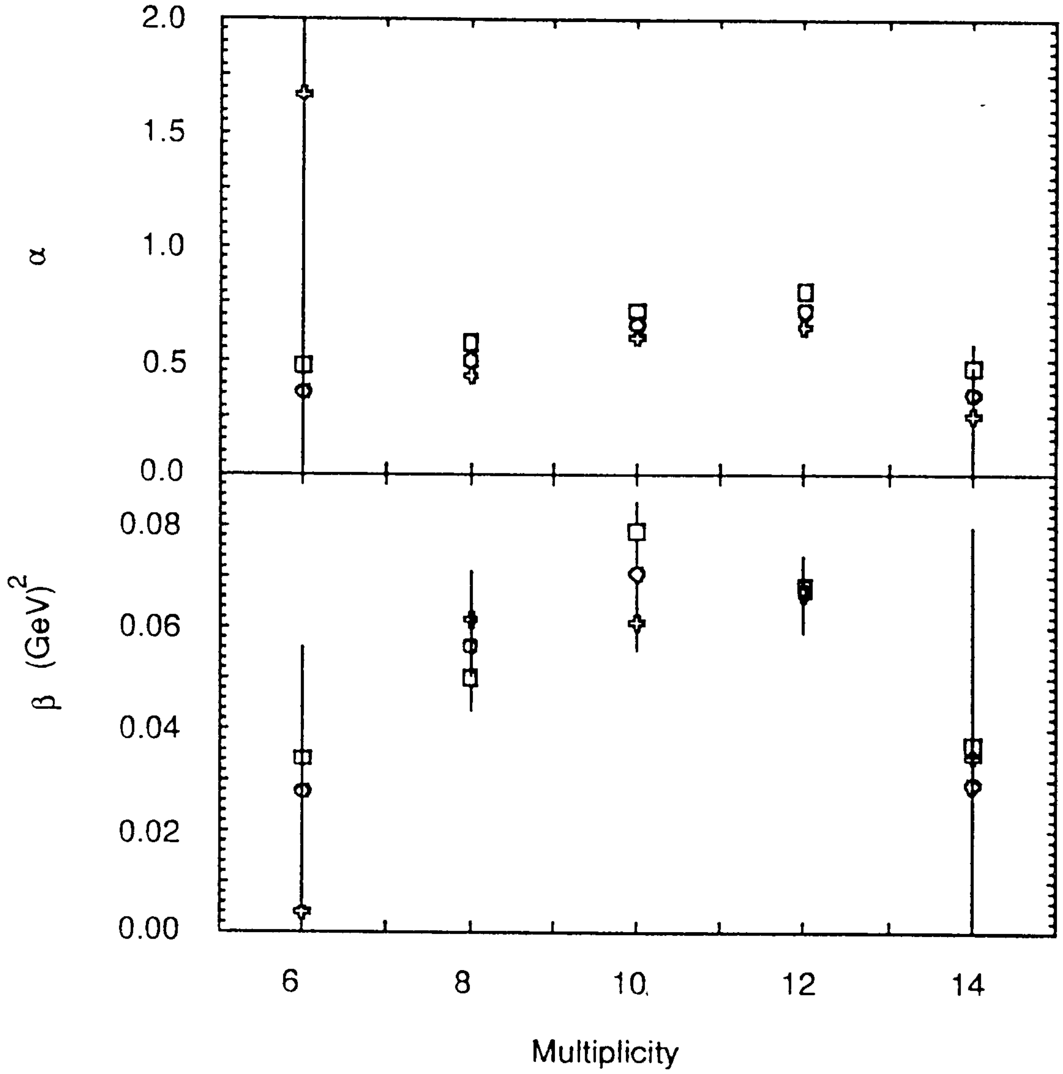
2.0
1.5
1.0
0.5
0.0
α
0.08
0.06
0.04
0.02
0.00
β (GeV)^2
6
8
10
12
14
Multiplicity

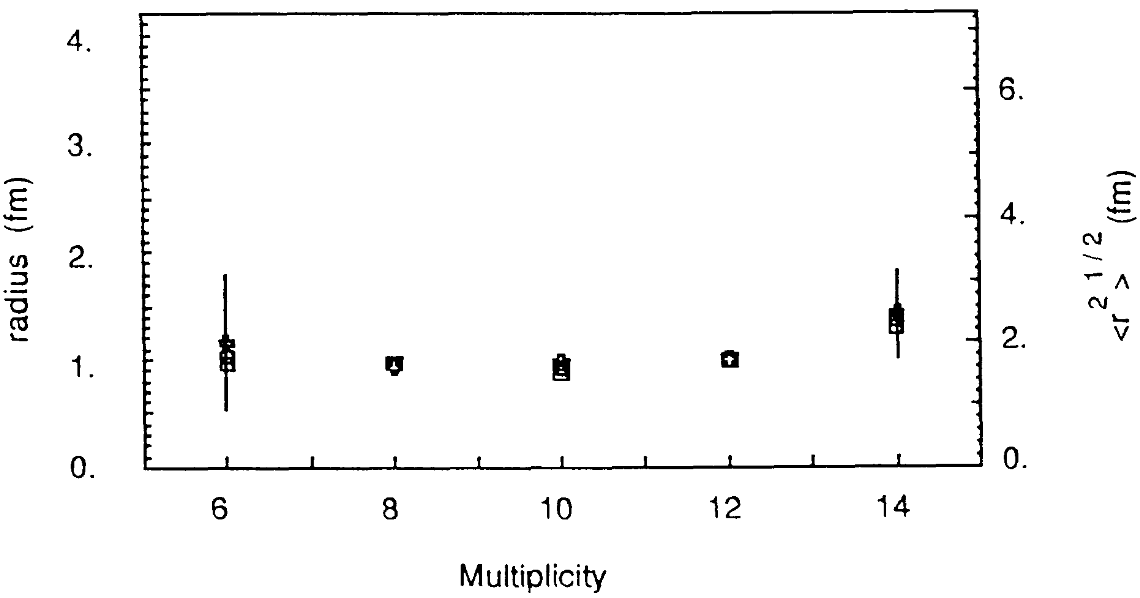
4.
3.
2.
1.
0.
radius (fm)
6.
4.
2.
0.
$<r^2>^{1/2}$ (fm)
6
8
10
12
14
Multiplicity

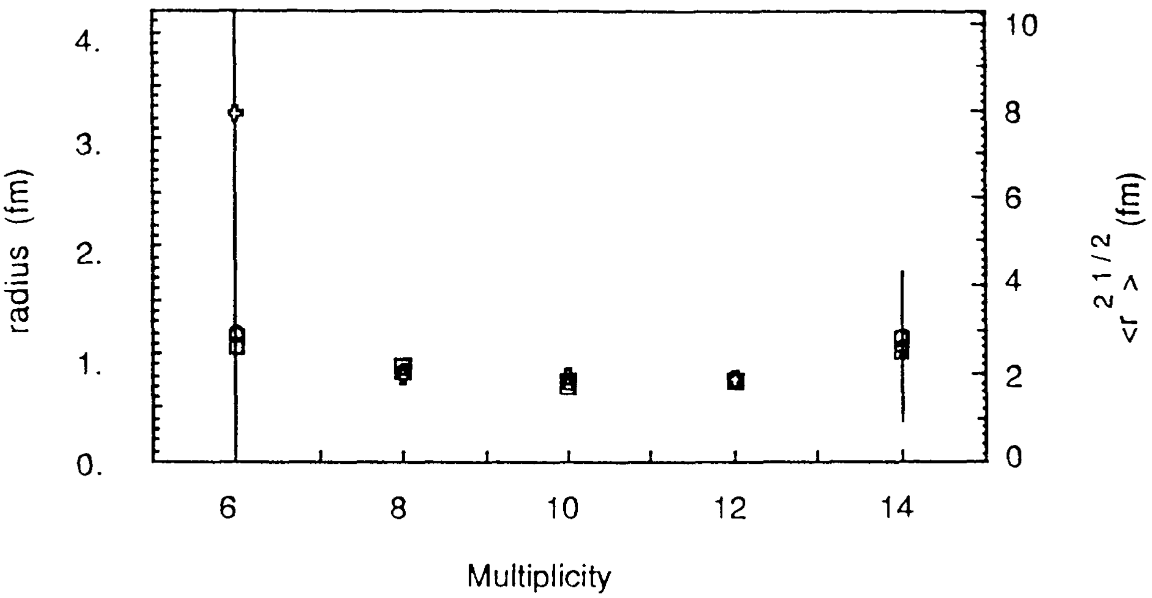

radius (fm)
4.
3.
2.
1.
0.
10
8
6
4
2
0
$<r^2>^{1/2}$ (fm)
6
8
10
12
14
Multiplicity

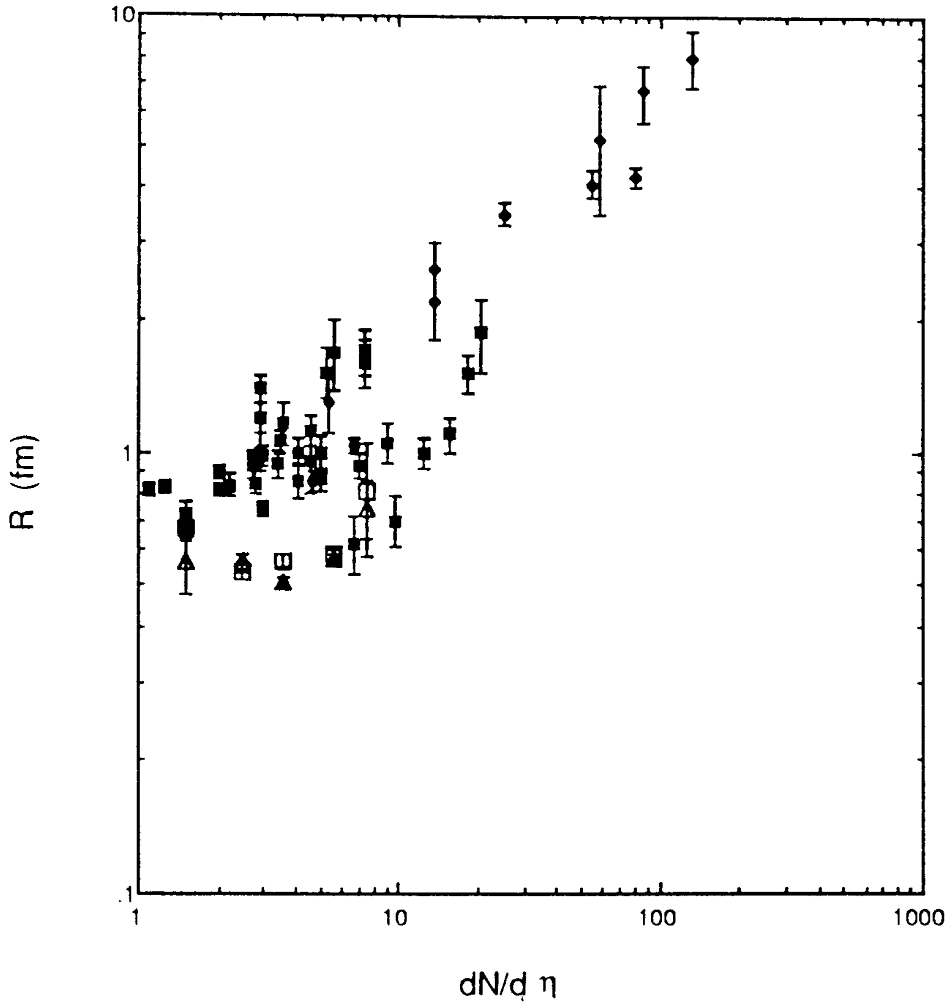

10
1
.1
1
10
100
1000
R (fm)
dN/d η